The loader complex Scc2/4 forms co-condensates with DNA as loading sites for cohesin

Sarah Zernia[1], Dieter Kamp[1], Johannes Stigler[1,*]

[1] Gene Center Munich, Ludwig Maximilian University, Feodor-Lynen-Strasse 25, 81377 Munich, Germany

* corresponding author

The genome is organized by diverse packaging mechanisms like nucleosome formation, loop extrusion and phase separation, which all compact DNA in a dynamic manner. Phase separation additionally drives protein recruitment to condensed DNA sites and thus regulates gene transcription. The cohesin complex is a key player in chromosomal organization that extrudes loops to connect distant regions of the genome and ensures sister chromatid cohesion after S-phase. For stable loading onto the DNA and for activation, cohesin requires the loading complex Scc2/4. As the precise loading mechanism remains unclear, we investigated whether phase separation might be the initializer of the cohesin recruitment process. We found that, in absence of cohesin, budding yeast Scc2/4 forms phase separated co-condensates with DNA, which comprise liquid-like properties shown by droplet shape, fusion ability and reversibility. We reveal in DNA curtain and optical tweezer experiments that these condensates are built by DNA bridging and bending through Scc2/4. Importantly, Scc2/4-mediated condensates recruit cohesin efficiently and increase the stability of the cohesin complex. We conclude that phase separation properties of Scc2/4 enhance cohesin loading by molecular crowding, which might then provide a starting point for the recruitment of additional factors and proteins.

Introduction

In eukaryotic interphase cells, DNA is folded and condensed to fit into the confines of the nucleus. This folding needs to be dynamic to allow biochemical reactions like DNA replication, repair, recombination or transcription to occur. DNA is folded into nucleosomes forming a beads-on-a-string-like structure, which compacts DNA around sevenfold (Oudet et al., 1975). Different histone modifications furthermore regulate accessibility of the DNA leading to the less densely packed gene-rich euchromatin and the more densely packed transcriptional inactive heterochromatin (Y. Kim & Yu, 2020). Additionally, the chromatin fiber is folded by loop formation into topologically associated domains (TADs), which exhibit high self-interaction and bring far-distance regions of the genome into close proximity (Dixon et al.,

34   2012; Fudenberg et al., 2016; Pombo & Dillon, 2015). This formation of spatially organized structures
35   promotes contacts between enhancers and promoters and is tightly linked to gene regulation (Pope et
36   al., 2014; Szabo et al., 2019).

37   With its apparent ability to extrude loops of DNA, the cohesin complex is one of the key proteins in TAD
38   formation (Davidson & Peters, 2021; Fudenberg et al., 2017). Furthermore, cohesin establishes sister
39   chromatid cohesion (Guacci et al., 1997; Michaelis et al., 1997) most likely by simultaneously entrapping
40   two DNA strands (Haering et al., 2008). To stably load onto DNA, cohesin requires a loader complex,
41   called Scc2/4 in budding yeast (Ciosk et al., 2000; Collier et al., 2020; Murayama & Uhlmann, 2014).
42   This heterodimer is shaped like a hook, provides two interaction sites for DNA (Kurokawa & Murayama,
43   2020) and can clamp cohesin on DNA by interfacing with all cohesin subunits (Chao et al., 2015; Higashi
44   et al., 2020), which leads to increased lifetime of cohesin on DNA (Gutierrez-Escribano et al., 2019;
45   Stigler et al., 2016). However, the cohesin-Scc2/4 interaction seems to be relatively transient as Scc2/4
46   was found to hop between different cohesin complexes (Rhodes et al., 2017) and is counteracted by
47   Pds5 (Kikuchi et al., 2016; Petela et al., 2018) as well as Wapl (Haarhuis et al., 2017). Besides simple
48   DNA clamping, Scc2/4 can stimulate the ATPase function of cohesin's head domains leading to ATP
49   hydrolysis, which is necessary for DNA entrapment inside the cohesin ring (Çamdere et al., 2015;
50   Murayama & Uhlmann, 2014; Petela et al., 2018). Recently, it was found that Scc2/4 can bind to
51   different sites of the cohesin ring, dependent on ATP, suggesting a two-step loading mechanism
52   initialized by ATP-independent binding at the hinge region followed by a transition towards the ATPase
53   head domains (Bauer et al., 2021). However, it remains unclear what initializes and drives the loading
54   process.

55   Real-time single-molecule experiments have revealed that cohesin forms both DNA loops (Davidson et
56   al., 2019; Y. Kim et al., 2019) and trans-tethers of DNA (Gutierrez-Escribano et al., 2019), exclusively
57   in the presence of Scc2/4. Additionally, these experiments have shown that cohesin can unspecifically
58   compact DNA (Gutierrez-Escribano et al., 2019), even across nucleosomes (Y. Kim et al., 2019), which
59   is caused by the formation of large protein-DNA-co-condensates with liquid-like properties (Ryu et al.,
60   2021). Phase separation was shown before to be an important mechanism in genome organization as
61   it forms regions of increased protein and DNA concentration to facilitate for example gene transcription
62   activation or repression (Boehning et al., 2018; Boija et al., 2018; Kent et al., 2020; Larson et al., 2017;
63   Sabari et al., 2018; Strom et al., 2017). Furthermore, other DNA-binding proteins like HP1α (Keenen et
64   al., 2020) and FUS (Zuo et al., 2021) were previously found to compact DNA by phase separation in a
65   comparable fashion.

66   The requirement of Scc2/4 for the formation of cohesin-DNA co-condensates raises the question
67   whether phase separation is not only an essential process for DNA organization but could also
68   contribute to the cohesin loading process. To our surprise, we found that Scc2/4 alone is able to phase
69   separate on DNA curtains and can form microscopic co-condensates with DNA in a concentration-
70   dependent manner. We characterized these condensates in terms of preconditions, stability,
71   reversibility and dynamics using DNA curtains and optical tweezers and found that Scc2/4 serves as a
72   DNA bridging factor. Finally, we document preferred cohesin loading at Scc2/4-DNA-co-condensates

73   and higher cohesin stability when it is loaded at these sites, suggesting a loading mechanism primed

74   by phase separation.

Results

The cohesin loader Scc2/4 connects and compacts DNA molecules

77   To visualize the effects of the cohesin loader Scc2/4 on DNA, we immobilized ~48.5 kbp dsDNA

78   molecules derived from bacteriophage lambda to a lipid bilayer in a flow chamber that allowed us to

79   exchange buffer components (see **Fig. S1A**). The YOYO-1-stained DNA molecules could diffuse freely

80   in the absence of buffer flow (**Fig. 1A**). Upon injection of 8 nM Scc2/4, we observed the slow formation

81   of puncta on the surface (**Fig. 1A**) that increased in fluorescence and compacted in size over time

82   (**Fig. S1B,C**). The formation was strictly dependent on the presence of Scc2/4. Intrigued by this, to our

83   knowledge, previously undescribed coagulation of DNA into clustered condensates by Scc2/4, we

84   decided to characterize the properties and consequences of this phenomenon in more detail.
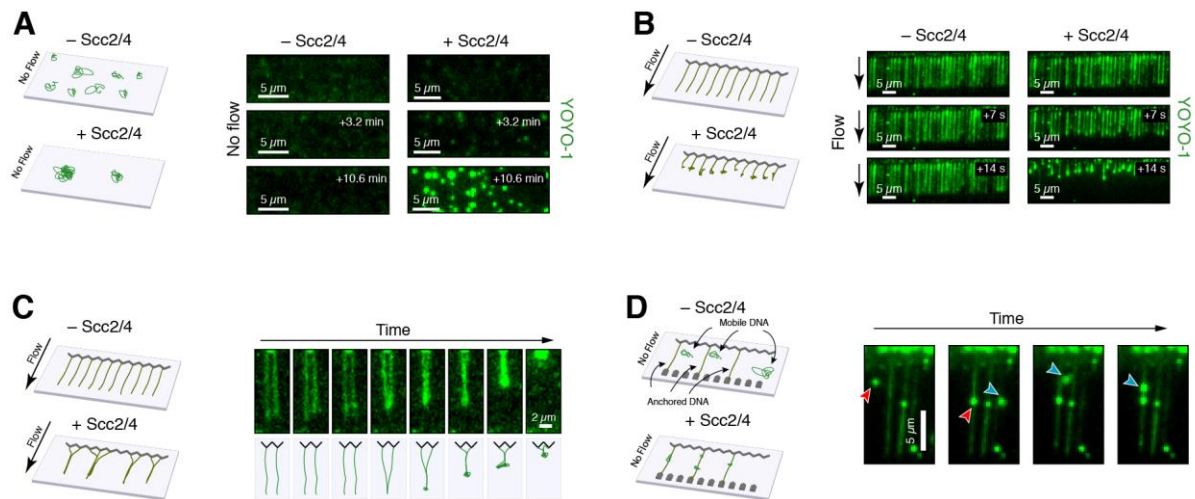
85
86   **Figure 1.** The cohesin loader Scc2/4 condenses and compacts DNA. (**A**) Diffusing DNA molecules, tethered to a

87   lipid bilayer, form condensates after addition of 8 nM Scc2/4. (**B**) DNA curtains assay of flow-stretched DNA.

88   Addition of 100 nM Scc2/4 leads to rapid compaction. (**C**) Braiding between neighboring flow-stretched DNA

89   strands after Scc2/4 addition. (**D**) Mobile lipid-anchored DNA molecules (red and blue arrows) attach to double-

90   tethered DNA molecules after Scc2/4 addition in the absence of flow.

91   Thus, we used single-tethered DNA curtains (Greene et al., 2010), where lipid-attached lambda DNA

92   is flow-stretched across nanofabricated barriers allowing the investigation of multiple DNA molecules in

93   an array format (**Fig. 1B**). While flow-stretched DNA remained at full length in the absence of Scc2/4,

94   we observed rapid shortening and compaction of DNA upon the injection of 100 nM Scc2/4 (**Fig. 1B**).

95   In a similar setting, we also observed Scc2/4-dependent braiding of adjacent DNA molecules, which

96   typically started from the free end, followed by compaction (**Fig. 1C**), indicating that Scc2/4-mediated

97   interactions led to both the coagulation of DNA molecules in trans as well as in cis. This protein-

98   dependent formation of DNA clusters and tethering in trans was also apparent in double-tethered DNA

99   curtains, where we observed an Scc2/4-dependent recruitment of mobile lipid-anchored DNA molecules

100   (red and blue arrows in **Fig. 1D**) to stretched surface-anchored DNA molecules.

Large-scale co-condensation of Scc2/4 with DNA occurs at physiological conditions

102   Co-condensation of nucleic acids with proteins has mainly been described and observed by the

103   formation of macroscopic phase-separated droplets in solution (Keenen et al., 2020; Morin et al., 2020;

104   Zhou et al., 2019; Zuo et al., 2021). To test whether Scc2/4-DNA co-condensates also form phase-

105   separated droplets, we titrated varying concentrations of Scc2/4 to a 30 nM solution of DNA fragments

106   of ~2.9 kbp and checked for condensate formation by bright-field microscopy. Strikingly, we observed

107   the formation of visible phase-separated droplets in an Scc2/4-concentration-dependent manner, with

108   droplets appearing at concentration above 300 nM Scc2/4 (**Fig. 2A**). Note that condensates exclusively

109   formed in presence of DNA. We therefore conclude that the observed clustering, coagulation and

110   compaction of single DNA molecules is, in fact, co-condensation of Scc2/4 and DNA.
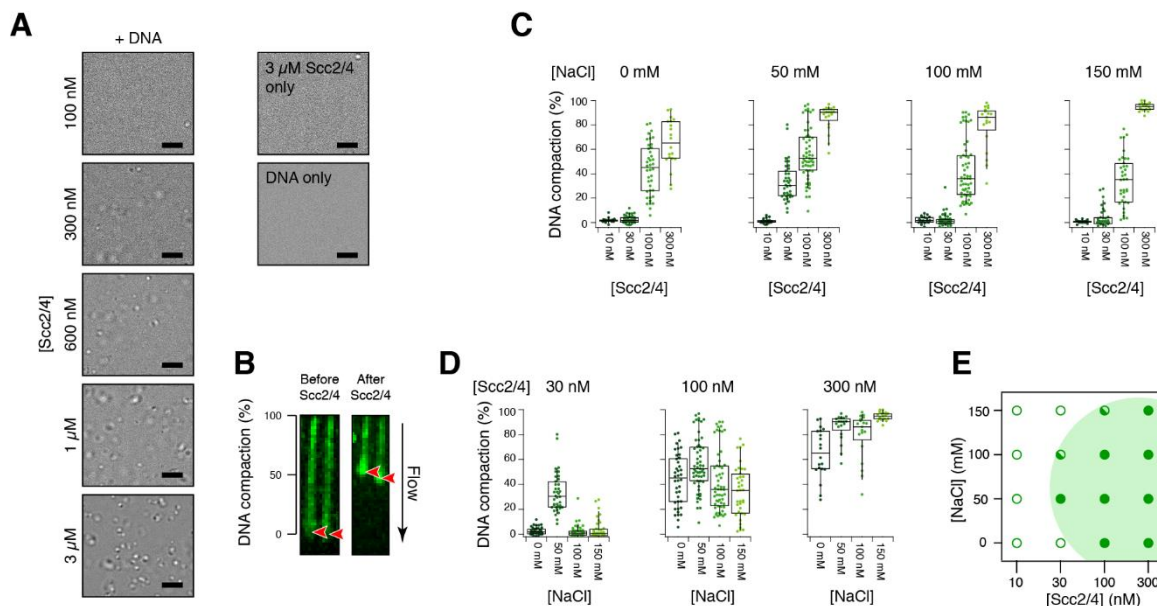
111

112   **Figure 2.** Quantification of DNA condensation from single molecule and bulk microscopy experiments. (**A**) Bright-

113   field microscopy images of large co-condensates of Scc2/4 and 30 nM 2686 bp DNA fragment. Scale bar: 10 µm.

114   (**B**) Example of DNA compaction by short pulses of Scc2/4. Red arrows show the free DNA end before and after

115   compaction. (**C**) Compaction of single lambda DNA molecules after injection of 50 µl pulses of Scc2/4 at the

116   indicated concentrations, at varying concentrations of NaCl. For 10 nM and 300 nM pof Scc2/4, 19 DNA strands

117   were analyzed, for 30 nM and 100 nM, 38 DNA strands were analyzed. (**D**) Rearranged data of (**C**) showing an

118   optimal salt concentration for condensation. (**E**) Phase diagram of DNA condensation from single molecule

119   experiments. Open circles: no condensation; closed circles: condensation, half-filled circles: condensation occurred

120   occasionally. The green area in the background represents the range where condensation was observed, to guide

121   the eye.

122   To further explore the range of concentrations that led to the co-condensation of single DNA molecules,

123   we returned to DNA curtain experiments. We injected 50 µl volumes of varying concentrations of Scc2/4

124   into a DNA curtain flow chamber with a flow rate of 0.1 ml/min, which exposed DNA to protein for ~60 s

4

125 (**Fig. S2A**). We then determined the degree of DNA compaction by measuring the DNA length before
126 and after Scc2/4-exposure (**Fig. 2B**). The compaction was positively correlated with the concentration
127 of Scc2/4 (see also **Fig. S2B** for examples of DNA compaction). While at 10 nM Scc2/4 the DNA
128 remained essentially fully extended, 300 nM Scc2/4 compacted the DNA almost completely (**Fig. 2C**).
129 We note that the reported Scc2/4 concentrations should be compared only within the context of the
130 flow-stretched compaction assay. Lower concentrations still may induce condensation on relaxed DNA,
131 albeit with a longer time constant (e.g. **Fig. 1A**). As protein-DNA co-condensation often relies on
132 electrostatic interactions (Erdel & Rippe, 2018), we tested the influence of monovalent salt on DNA
133 compaction by varying the NaCl concentration between 0 mM and 150 mM. However, while compaction
134 was significantly enhanced at 50 mM NaCl, the overall dependency on salt concentration was weak
135 (**Fig. 2C,D**). The data is summarized in the phase diagram of **Fig. 2E**, showing the range of Scc2/4 and
136 NaCl concentrations where the formation of co-condensates was observed. Importantly, we observed
137 significant compaction of DNA at near physiological salt (150 mM NaCl) and Scc2/4 concentrations
138 (~300 nM, (Ho et al., 2018), **Fig. 2C**, right), suggesting that Scc2/4-mediated DNA condensation may
139 also occur in vivo.

Scc2/4 serves as a DNA-bridging factor in condensates

141 Intrigued by the observation that the cohesin loader Scc2/4 can lead to the formation of DNA-DNA
142 contacts on its own, without the help of the SMC complex cohesin, we next sought to characterize the
143 mechanism of Scc2/4-mediated DNA condensate formation in greater detail. Condensation of
144 biomolecules generally requires binding multivalency of the condensate components. Many phase
145 separating proteins cluster by homo-interactions through intrinsically disordered domains (IDRs), which
146 form a molten-globule-like state through hydrophobic interactions by excluding water molecules (LLPS,
147 liquid-liquid phase separation, (Dignon et al., 2020; Erdel & Rippe, 2018; Razin & Ulianov, 2020)).
148 However, prediction software does not indicate that there are extended IDRs in Scc2/4 (the unstructured
149 N-terminus of Scc2 is structured upon binding of Scc4, **Fig. S3**). In agreement with this assessment,
150 washes with 20 % 1,6-hexanediol, a strong disruptor of hydrophobic interactions that has been used
151 extensively in studies of LLPS (Ladouceur et al., 2020; Ryu et al., 2021), was not able to decondense
152 Scc2/4-DNA co-condensates (**Fig. 3A**). In contrast, disruption of electrostatic interactions, such as the
153 injection of 2M NaCl readily dissolved Scc2/4-DNA co-condensates and returned the DNA back to its
154 extended form (**Fig. 3B**). We conclude that the co-condensation mechanism between Scc2/4 and DNA
155 is likely driven by electrostatic rather than hydrophobic interactions.

156 Contrasting the LLPS model, our findings are instead compatible with the electrostatics-dependent
157 mechanism of polymer-polymer phase separation (PPPS, (Erdel & Rippe, 2018)), which entails the
158 bridging of polymers (DNA) through multivalent proteins (Scc2/4). As the PPPS mechanism additionally
159 predicts that free protein is required to induce the formation of condensates we tested this possibility in
160 pulsed injection experiments, where we injected short 50 µl pulses of 30 nM Scc2/4 onto a dsDNA
161 curtain that was stretched at a flow rate of 0.1 ml/min. Intriguingly, we found that the condensation of
162 DNA only proceeded while Scc2/4 was present in the flow cell and stopped after free Scc2/4 had been
163 washed out (**Fig. 3C**), resulting in a DNA-Scc2/4 co-condensate at the end of the DNA. We tested if

164　condensates at the end of the DNA are capable of recruiting additional DNA, even in the absence of

165　free Scc2/4, by stopping the flow and allowing the DNA to relax. However, we found that in repeated

166　flow on/off cycles, the length of the condensed DNA remained the same (**Fig. 3D**). While condensate

167　sizes remained stable in absence of free Scc2/4, condensation readily restarted when additional pulses

168　of free Scc2/4 were injected into the flow cell (**Fig. 3E**) and existing condensates were then also able

169　to fuse (**Fig. S2D**). We also observed merging and coalescence of freely diffusing lipid-bilayer-anchored

170　DNA-Scc2/4 condensates in presence of free Scc2/4 (**Fig. 3F**). Hence, we conclude that the formation

171　of Scc2/4-mediated DNA condensates requires free Scc2/4 as a DNA bridging factor, which fulfills the

172　characteristics of PPPS.
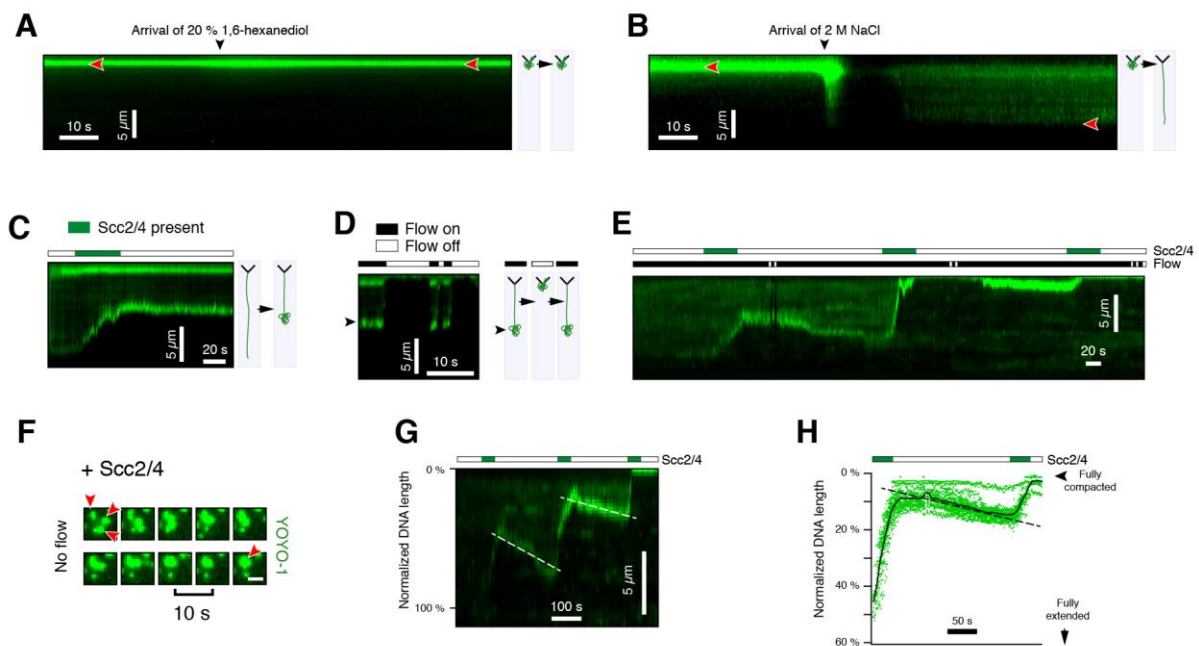
173

174　**Figure 3.** DNA condensation and decondensation dynamics by Scc2/4. (**A+B**) Kymograms of an Scc2/4-induced

175　condensate on a single DNA molecule, challenged with 20% 1,6-hexanediol (**A**) or 2 M NaCl (**B**). Red arrows

176　indicate the free end. (**C**) Kymogram of flow-stretched DNA upon injection of a short pulse of 100 nM Scc2/4. The

177　DNA condenses only while protein is in the flow chamber (green bar indicates protein presence). (**D**) In the absence

178　of Scc2/4 in the flow chamber, DNA does not condense further when it is allowed to relax by relieving the flow

179　tension. (**E**) Kymogram of a multi-pulse experiment. The DNA only condenses while Scc2/4 is in the buffer chamber

180　(indicated by green bar). (**F**) Multiple mobile lipid-anchored DNA molecules coagulate to form larger condensates

181　while Scc2/4 is present. (**G**) Condensation clusters are reversible. DNA compacts while Scc2/4 is present in the

182　buffer chamber and slowly decompacts in the absence of Scc2/4. White lines indicate the end of the DNA molecule.

183　(**H**) Decondensation of 52 DNA molecules between pulses of Scc2/4. Black line: mean. Dashed line:

184　decondensation trend to guide the eye.

185　## Condensates are dynamic and reversible

186　A biologically relevant Scc2/4-mediated DNA and chromatin condensation mechanism must be

187　reversible. In the previously described experiments we have shown that condensates are static in the

188　absence of protein, i.e., they do not condense further. When we exposed partially condensed DNA to

189　long washes with buffer in the absence of free Scc2/4, we observed reproducible slow decondensation

6

190 and concurrent lengthening of DNA (**Fig. 3G**, white dashed line). DNA condensed in the presence of
191 Scc2/4 and decondensed in its absence, indicating that Scc2/4-mediated DNA condensates are
192 thermodynamically reversible. In a buffer flow of 0.1 ml/min, the decondensation rate was ~3%/min
193 (**Fig. 3H**).

Condensation is primarily driven by random collisions

195 DNA compaction as a precursor to condensate formation can occur through loop formation by active,
196 energy-consuming translocation of DNA binding factors (Goloborodko et al., 2016), but also by passive
197 mechanisms like DNA bridging, bending or wrapping (Johnson et al., 2008). The cohesin loader Scc2/4
198 has no known nucleotide hydrolysis activity and we found no significant influence of ATP on DNA
199 compaction by Scc2/4 (**Fig. S2C**), ruling out active processes. We, therefore, further explored the
200 possible mechanisms for passive DNA compaction. As in previous experiments, we used DNA curtains
201 and exposed single-tethered, flow-stretched 48.5 kbp DNA molecules to near-physiological
202 concentrations of Scc2/4. We followed the DNA compaction over time by observing the accumulation
203 of the YOYO-1 signal. A kymogram of a typical compaction curve for 100 nM Scc2/4 (**Fig. 4A**) shows
204 the appearance of a bright spot at the free end of the DNA, which gradually moves closer towards the
205 tethered end. This indicates that the compaction primarily starts at the free end. Intensity profiles along
206 the DNA at various time points (**Fig. 4B**) also confirm the appearance of a DNA condensate at the free
207 end. Interestingly, when we measured the fluorescence intensity upstream of the compacting end
208 (**Fig. 4C**), we found that it remained not constant but increased almost linearly as the DNA compacted
209 (**Fig. 4D**). This indicates that there is also internal compaction distant from the free end.

210 To more thoroughly distinguish potential mechanisms of compaction from the end (e.g., through the
211 capture of randomly fluctuating loops) or compaction everywhere (e.g. by bending), we used tracer
212 proteins to track the position of various positions along the DNA during compaction (H. Kim & Loparo,
213 2016). Generally, in a scenario where compaction occurs solely from the end, we expect that the inner
214 tracer molecules are static until they encounter the compacting end (**Fig. 4E**). On the contrary, a
215 scenario where compaction occurs everywhere predicts movement of internal tracers as soon as the
216 DNA is exposed to the compacting factor. **Fig. 4F** shows a representative kymogram of the Scc2/4-
217 mediated compaction of lambda DNA with Qdot-labeled EcoRI-E111Q tracer molecules bound.
218 Tracking of the tracer molecules then allowed us to follow the compaction path (**Fig. 4G**). To our
219 surprise, we found that, while our observations primarily corresponded to the scenario of compaction
220 from the end, the internal tracer proteins also started moving as soon as the DNA is exposed to Scc2/4
221 (red arrow in **Fig. 4G**, **Fig. S4B**). This indicates that while capture of freely fluctuating DNA loops at the
222 free end is the primary mechanism for DNA compaction and condensation, there is also a smaller
223 contribution of internal compaction, perhaps through DNA bending.
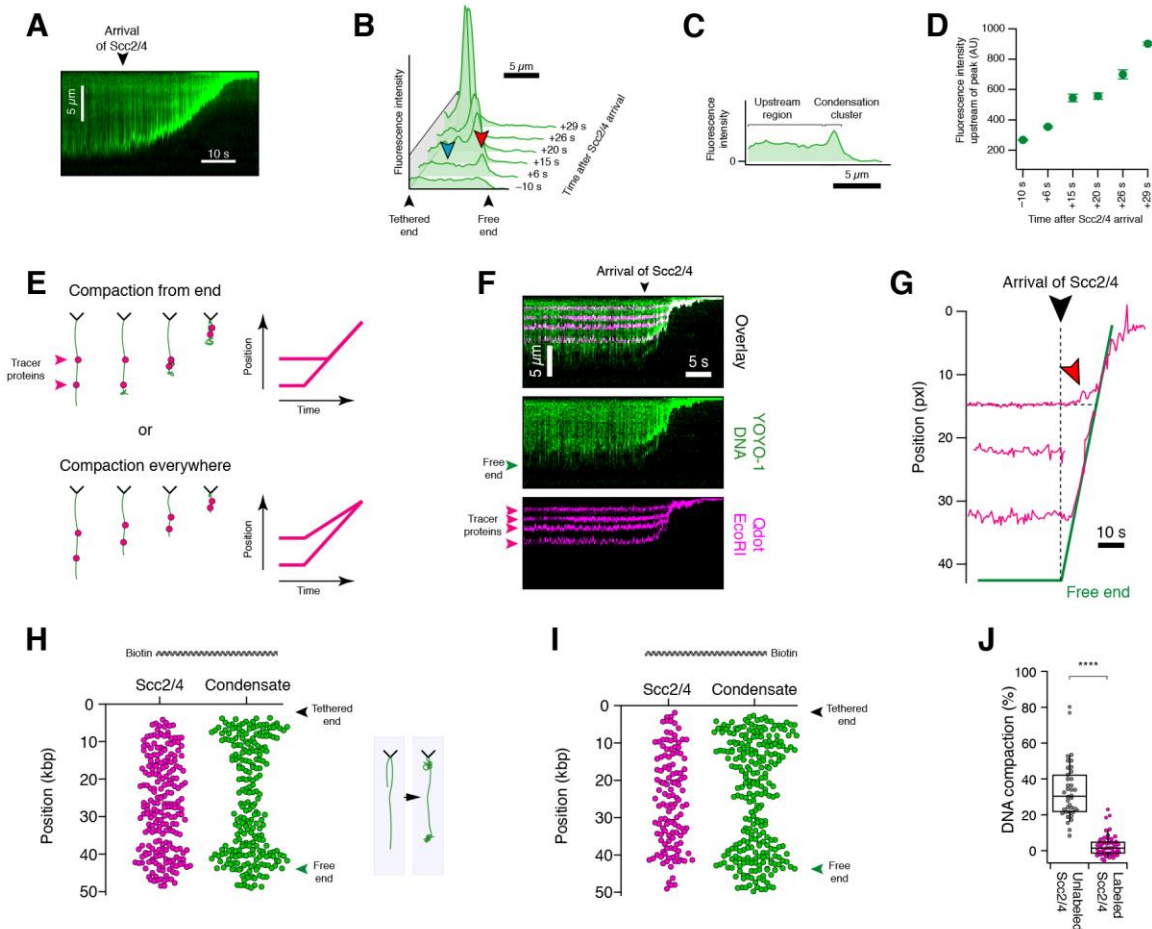
Figure 4. Direction of DNA compaction. (**A**) Kymogram of Scc2/4-mediated DNA condensation shows the appearance of a bright spot at the free end. (**B**) YOYO-1 intensity profiles of a single lambda DNA molecule during Scc2/4-mediated condensation. Time marks indicate the time after the start of Scc2/4 arrival in the flow cell. Red arrow: Condensate at the free end. Blue arrow: Region upstream of condensate. (**C**) YOYO-1 intensity profile along a single lambda DNA molecule during Scc2/4-mediated condensation. (**D**) Average YOYO-1 intensity of the region upstream of the free end (see blue arrow in (**B**)). (**E**) Models for the condensation of DNA. (**F**) Kymograms of Scc2/4-mediated condensation of lambda DNA, which was marked with fluorescently tagged EcoRI-E111Q tracer proteins. (**G**) Tracked positions of tracer proteins upon Scc2/4 addition. The red arrow shows movement of an internal tracer far away from the condensing end. (**H**) Binding positions of Qdot-tagged Scc2/4 (magenta) show a homogenous binding preference across the substrate. Condensation clusters (green) primarily occur at the free end as well as close to the barriers. Data points were pooled from two independent experiments. (**I**) Experiment as in (**G**), with DNA that was tethered at the opposite end. Data points were pooled from three independent experiments. (**J**) DNA compaction of 30 nM unlabeled or labeled Scc2/4. For unlabeled and labeled protein binding, 38 and 50 DNA strands were analyzed, respectively. Distribution is according to student's t-test significantly different.

We further considered the possibility that the movement of internal tracer molecules could also be a consequence of altered hydrodynamic properties of the DNA during apparent shortening in flow. To address this question, we turned to coarse-grained molecular dynamics simulations where lambda DNA is represented by a Rouse model of 160 beads that were connected by segments of ~300 bps in length while internal compaction was excluded. After applying flow stretching forces (**Fig. S4C, left**), we

8

245   modeled the effect of Scc2/4 by introducing an attractive Lennard-Jones-like potential between the

246   beads (see Methods), which explicitly did not induce a shortening of segments but nevertheless led to

247   a rapid compaction of the modeled DNA (**Fig. S4C, right**) due to condensation at the free end. In

248   contrast to DNA curtain experiments, these simulations did not display the movement of internal tracer

249   molecules until they were encountered by the condensing end. This suggests that the experimentally

250   observed movement of tracers is not caused by a change in hydrodynamics but indeed by internal

251   compaction or bending of DNA initiated by Scc2/4 binding.

252   Finally, we asked if end-dependent compaction may be caused by preferred association of Scc2/4 to

253   free ends. To this end, we Qdot-labeled Scc2/4 and tracked the binding position of Scc2/4 before the

254   onset of condensation (**Fig. 4H**). While DNA condensates initially formed primarily at the free end, the

255   binding position of Scc2/4 showed no preference. We obtained the same result when we anchored the

256   DNA molecule at the opposite end suggesting sequence-independent binding (**Fig. 4I**). In both

257   orientations we also observed a fraction of condensate clusters close to the tethered end, which we

258   attribute to the presence of shorter DNA molecules. However, while Qdot-labeled Scc2/4 was clearly

259   able to bind DNA, labeling had a partially disruptive effect on DNA-compaction (**Fig 4J**), plausibly

260   through interfering with at least one of Scc2/4's DNA binding sites.

Scc2/4 compacts DNA by a tension-dependent bridging mechanism

262   To unravel what drives Scc2/4-mediated bridging on DNA, we utilized optical tweezers and first studied

263   the influence of DNA tension on Scc2/4 interaction. A single lambda DNA molecule was tethered

264   between two optically trapped beads, which allows force application and measurement in a very

265   accurate manner. We incubated the DNA with 10 nM of Scc2/4 first in a tensioned (7.5 µm bead

266   distance) and then in a more relaxed conformation (5 µm bead distance, **Fig. 5A**, **Fig. S5B**) and found

267   in both cases a strong gradual increase in force due to protein association to the DNA (**Fig. 5B** magenta

268   trace, see also **Fig. S5A** for responses of individual tethers). Naked DNA (green) did not show a change

269   in force, while DNA that was transferred into buffer after protein incubation (black) displayed a slight

270   decrease in force due to unbinding of protein (**Fig. 5B**). To quantitate and compare the degree of

271   compaction at different tension, we calculated the apparent contour length of the tethers as a function

272   of time. Although compaction occurred at both incubation steps, Scc2/4-mediated compaction was

273   much stronger when DNA was held at 5 µm (**Fig. 5C**), where DNA is more relaxed and can be bridged

274   much easier (**Fig. 5A**).

275   Next, we wondered whether the condensates can be removed from DNA by increasing forces. We

276   applied five stretch and relax cycles to the DNA and recorded force-extension curves (FEC). We

277   observed a Scc2/4-dependent sawtooth pattern, which is a key characteristic of protein-mediated DNA

278   bridges that are ruptured at increasing forces (**Fig. 5D**). While most bridges could be resolved by

279   moderate tensions, we also observed bridges that resisted at forces up to ~65 pN, where the DNA

280   undergoes force-induced melting. Note, that broken bridges did not reform during relaxation of the DNA

281   strand (**Fig. 5D**), but readily re-formed on fully relaxed DNA, as evidenced by the reappearance of the

282   sawtooth pattern in subsequent cycles (**Fig. S5C**). Additionally, we recognized the absence of the

283   sawtooth pattern, when DNA was incubated at very high tension (14.4 µm bead distance) and directly

284   stretched (**Fig. 5E**). These results indicate that bridging requires relaxed DNA, but does not necessitate

285   the presence of a free DNA end.
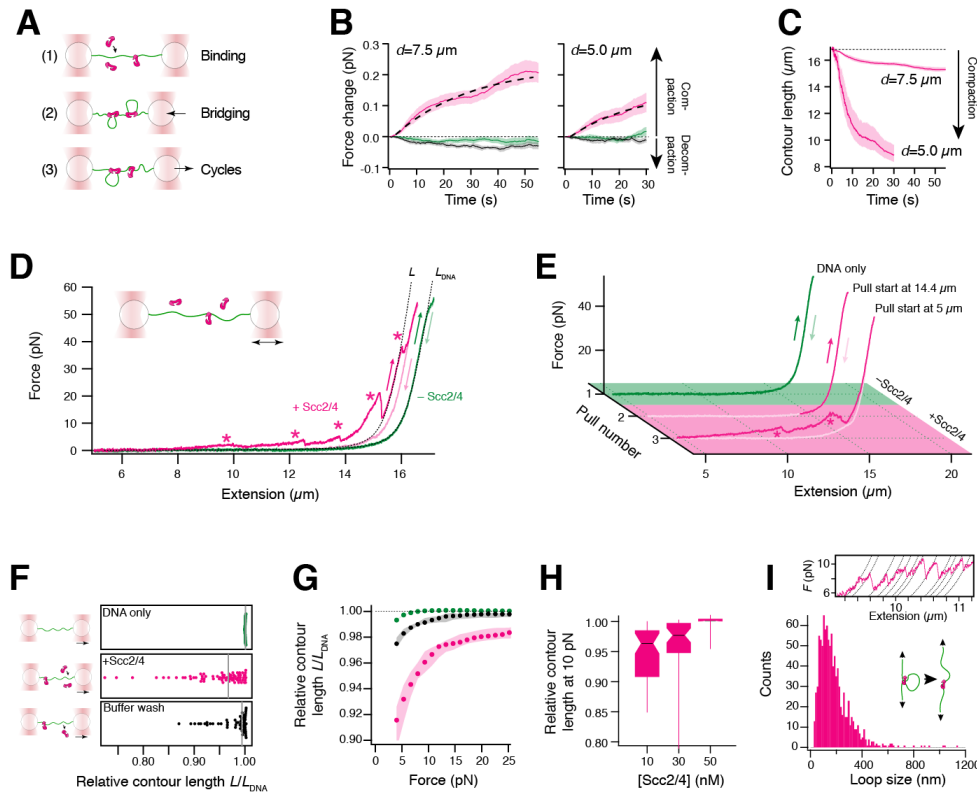
Figure 5. Optical tweezers experiments for understanding the DNA coagulation mechanism of Scc2/4. (**A**) Schematic representation of the experimental procedure. (**B**) Transient force response of DNA tethers held at the indicated distance in flow channels without Scc2/4 (green), with 10 nM Scc2/4 (magenta) or in a buffer channel after previous Scc2/4 incubation (black). Colored line represents the mean of 15 tethers, shading represents the SEM, dashed line represents an exponential fit. (**C**) Time-dependent reduction of the tether contour length in the presence of 10 nM Scc2/4. (**D**) Force-extension curves (FECs) of lambda DNA in the absence (green) and presence (magenta) of 10 nM Scc2/4. Darker shades are stretch traces, lighter shades are relaxation traces. Dashed lines indicate the expected force response of a full-length DNA or a DNA that is shortened by partial compaction, based on an eWLC model. (**E**) Subsequent pulls of lambda DNA that was transferred from the buffer channel (green) to the channel with 10 nM Scc2/4 (magenta). The DNA was incubated in the protein channel in an extended state (pull 2) or at a lower tension (pull 3). Observed compaction is marked by asterisks. (**F**) Relative contour length of DNA stretch-traces from multiple molecules at 10 pN, normalized to the expected contour length of lambda DNA. Green: In the absence of Scc2/4, magenta: In the presence of 10 nM Scc2/4, black: In the buffer channel, after previous Scc2/4 incubation. Grey lines indicate the median. (**G**) Median relative contour lengths of stretch traces at various forces. Shading indicates 68% confidence intervals from bootstrapping. Color code as in (**F**). (**H**) Relative contour lengths at 10 pN after incubation at different protein concentrations. Number of analyzed tethers 10nM: 15, 30 nM: 10, 50 nM: 13. (**I**) Determination of the length of opened loops from sawtooth features. Top: representative stretch FEC with eWLC fits to individual features. Bottom: histogram of loop lengths of 16 individual DNA tethers incubated with 10 nM Scc2/4.

306   We characterized the observed shortening of the DNA by comparing the relative DNA contour length

307   (L/L_{DNA}, see **Fig. 5F**) of naked DNA with DNA incubated in Scc2/4 and observed clear DNA compaction

308 in presence of Scc2/4, which was reduced to almost naked DNA level when washing the DNA in buffer
309 after protein incubation (**Fig. 5G**). When looking at individual cycles, we found the strongest compaction
310 for the first cycle, caused by the prior incubation step, while the other four cycles showed reduced but
311 constant compaction as proteins constantly bind and unbind (**Fig. S5D**). During the buffer wash,
312 compaction is reduced in each cycle due to continuous protein unbinding (**Fig. S5D**). We conclude that
313 DNA compaction by Scc2/4 is reversible and can be removed by buffer washes or mechanical tension.

314 Besides DNA tension, it is likely that also protein concentration influences DNA compaction. To
315 quantitate the dependency on protein concentration, we recorded FECs at increasing Scc2/4
316 concentrations and found, surprisingly, that compaction was reduced at 30 nM Scc2/4 and completely
317 vanished at 50 nM (**Fig. 5H**). Similarly, we also found that, during incubation, higher protein
318 concentrations counterintuitively resulted in less compaction (**Fig. S5E**). While this finding is puzzling
319 at first glance, it is compatible with the PPPS model of multivalent Scc2/4 bridging DNA: In the case of
320 high protein coverage, there are no more freely accessible DNA binding sites and additional bridges
321 are abrogated, resulting in less DNA compaction.

322 Finally, to quantify the size of DNA loops formed by bridging, we fitted extensible worm-like chain
323 (eWLC) models to individual rupture events in the sawtooth pattern of FEC and collected all loop sizes
324 in a histogram (**Fig. 5I**). The mean loop size of 183 ± 4 nm (~540 nt) suggested that DNA is not just
325 simply wrapped around Scc2/4 but bridged over longer distances.

Scc2/4-DNA co-condensates are preferred loading sites for cohesin

327 The stark compaction and condensation properties of Scc2/4 raise the possibility that the observed
328 behavior has direct consequences for Scc2/4's role as a loading factor for cohesin. To address this
329 question, we performed DNA curtain experiments where we pre-loaded 30 nM Scc2/4 to initiate
330 condensate formation followed by loading of 20 nM Qdot-labeled tetrameric cohesin (SMC1, SMC3,
331 SCC1, SCC3) with a continuous flow of 0.1 ml/min (**Fig. 6A**). After washing out all unbound protein, we
332 observed in ~70% of all cases that cohesin bound directly to Scc2/4-DNA co-condensates while the
333 other proteins attached to uncompacted regions of the DNA (**Fig. 6B**). Kymograms of the whole binding
334 process revealed that, apart from direct binding to the condensate or free DNA, some proteins also
335 initially associated to uncompacted DNA and then slid towards the condensates to stick there (**Fig. 6D**).
336 When incubating cohesin and Scc2/4 simultaneously for 10 min on DNA curtains we observed cohesin
337 overwhelmingly enriched at condensates (**Fig. S6A**). This suggests that most cohesins that initially
338 associated to uncompacted DNA did either dissociate or diffuse towards condensates during
339 incubation. In contract, when applying Qdot-labelled cohesin to a non-compacted, Scc2/4-free DNA
340 curtain (**Fig. S6C**), we observed eight times fewer binding events (**Fig. 6C**). These results show that
341 cohesin is preferably loaded on DNA via association with Scc2/4-formed condensates and that binding
342 is strongly enhanced through this process.

343 Furthermore, we tested whether the recruitment observed in this assay constitutes bona fide loading of
344 cohesin. In vitro loading of cohesin had been tested and investigated by performing washes with high
345 concentrations of monovalent salt (Gutierrez-Escribano et al., 2019; Minamino et al., 2018; Murayama

346 & Uhlmann, 2014; Ryu et al., 2021). Recapitulating these experiments, we washed the DNA after

347 loading with 2M NaCl. As expected, we observed decondensation together with stretching of the DNA

348 (**Fig. 6E**). The salt wash removed 79 % of the bound cohesin complexes. However, 21 % resisted the

349 high salt conditions, indicating a strong interaction mechanism (**Fig. 6G**). In absence of Scc2/4, high

350 salt washes removed the bound cohesin complexes completely (**Fig. 6F,G**) showing that Scc2/4

351 effectively promotes the formation of salt-stable cohesin-DNA interactions. Intriguingly, cohesin that had

352 loaded at Scc2/4-DNA co-condensates exhibited a significantly higher resistance to salt washes (38 ±

353 8 % remaining) than cohesin that had loaded at uncondensed DNA (17 ± 4 %) (**Fig. 6H**). We conclude

354 that Scc2/4-mediated DNA co-condensates serve as preferred sites for stable cohesin loading.
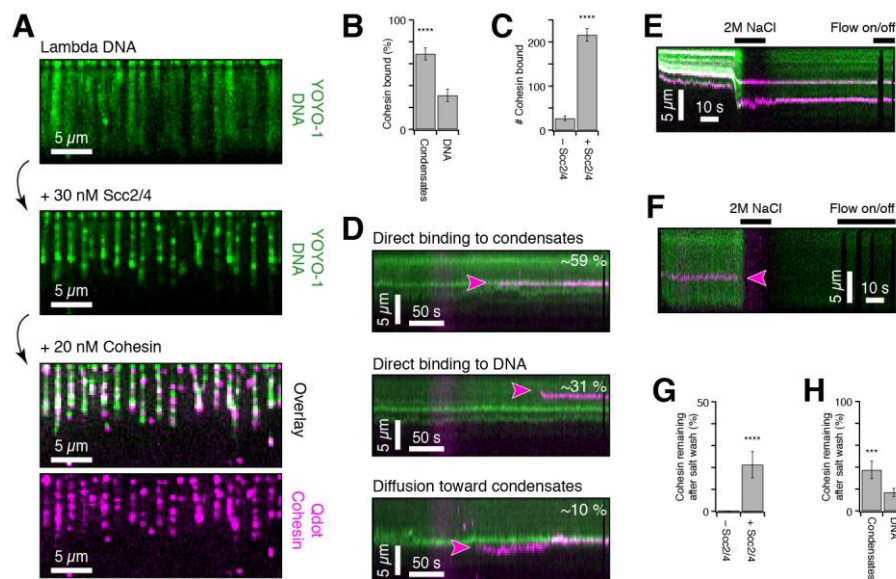
355

356 **Figure 6.** Scc2/4-mediated DNA condensates lead to enhanced loading of cohesin. (**A**) DNA curtain experiment of

357 Qdot-labeled cohesin (magenta) on Scc2/4-mediated DNA condensates (green). (**B**) Ratio of bound cohesin at

358 condensates or at uncompacted DNA after unbound protein was washed out. (**C**) Number of bound cohesin in

359 absence or presence of Scc2/4. (**D**) Representative kymograms of cohesin binding directly to condensates, directly

360 to uncompacted DNA or diffusing towards condensates. (**E**) Kymogram of 2M NaCl wash after cohesin was loaded

361 in presence of Scc2/4. Cohesin remains bound while DNA is decompacted and clusters are dissolved. (**F**)

362 Kymogram of 2M NaCl wash after cohesin was loaded in absence of Scc2/4. Cohesin cannot stay bound on DNA

363 during salt wash. (**G**) Proportion of cohesin molecules remaining on the DNA after 2 M NaCl wash when loaded

364 with or without Scc2/4. (**H**) Proportion of cohesin molecules remaining on the DNA after 2 M NaCl wash when

365 loaded in presence of Scc2/4 at condensates or uncompacted DNA. (**B+C+G+H**) Data was pooled from three

366 independent experiments, error bars represent the standard error of a binominal distribution. Significance was

367 calculated by a z-test.

Discussion

369 Here, we have described and characterized a previously unreported property of the cohesin loader

370 Scc2/4. While co-condensation of Scc2/4 with DNA may be unexpected, phase separation phenomena

371 in the context of cellular and nuclear organization are, in fact, common. In the past years it has emerged

372 that phase separation is an important feature to organize the crowded interior of cells, to separate

373 counteracting reactants but also to pool interacting molecules (Erdel & Rippe, 2018). Besides the
374 formation of distinct phase separated bodies, like stress granules, p-bodies or nucleoli (Verdile et al.,
375 2019), phase separation also promotes chromatin organization (Gallego et al., 2020; Larson et al.,
376 2017; Strom et al., 2017) and regulation of processes like transcription (Boehning et al., 2018; Boija et
377 al., 2018; Kent et al., 2020; Sabari et al., 2018; Wei et al., 2020), replication (Parker et al., 2019) or
378 DNA repair (Kilic et al., 2019). In fact, the cohesin complex phase separates in presence of the loader
379 protein Scc2/4 (Ryu et al., 2021). Furthermore, ParB, a bacterial SMC loading factor (Minnen et al.,
380 2011; Sullivan et al., 2009), undergoes phase separation in vivo (Broedersz et al., 2014; Guilhas et al.,
381 2020) and in vitro (Madariaga-Marcos et al., 2019) suggesting that condensate formation might be a
382 general feature of SMC loading proteins.

Phase separation vs. aggregation

384 In this work, we have demonstrated that the loading complex Scc2/4 is able to bridge and compact DNA
385 into protein-DNA co-condensates independently of cohesin. Previous studies did not investigate full-
386 length Scc2/4 alone and have used protein concentrations in the low nanomolar range leading to only
387 rarely observed protein clusters, which were often attributed to aggregation or impurities (Davidson et
388 al., 2019; Gutierrez-Escribano et al., 2019; Y. Kim et al., 2019). Our findings extend to physiological
389 protein and salt concentrations (300 nM Scc2/4 (Ho et al., 2018), 150 mM NaCl), strongly suggesting
390 that the observed phenomenon is also relevant in vivo. The presented results are compatible with well-
391 known hallmarks of phase separation (Mitrea et al., 2018), as the condensates exhibit liquid-like
392 behavior represented by droplet formation in bulk (**Fig. 2A**), fusibility in the presence of protein (**Fig.
393 3F, Fig. S2D**) and decomposition of condensates caused by exchange with the environment (**Fig. 3G**).
394 Condensate dynamics and reversibility also rule out the possibility that condensation may be triggered
395 by protein aggregation.

Protein constituents for generating phase separation

397 Many phase separating proteins contain intrinsically disordered regions (IDR) which promote high levels
398 of self-interaction and crowding (André & Spruijt, 2020) and lead to liquid-liquid phase separation
399 (LLPS). Scc2/4 lacks IDRs but comprises HEAT-repeats, which were found before to induce phase
400 separation (Aktar et al., 2019) due to their amphiphilic and very flexible structure (Kappel et al., 2010;
401 Yoshimura & Hirano, 2016). However, we propose that the observed Scc2/4-DNA co-condensates are
402 formed by polymer-polymer phase separation (PPPS), where Scc2/4 serves as a multivalent bridging
403 factor for DNA and does not self-interact. In our droplet experiments, both polymers, DNA and Scc2/4,
404 are required to form liquid-like droplets (**Fig. 2A**), which corroborates a PPPS-based mechanism. PPPS
405 has previously been shown for the related SMC loading factor ParB, which bridges DNA by multiple
406 helix-turn-helix motifs and also does not self-interact (Fisher et al., 2017; T. G. W. Graham et al., 2014).
407 DNA decondensation during salt wash (**Fig. 3B**) revealed that DNA bridging is promoted by electrostatic
408 rather than hydrophobic interactions (Erdel & Rippe, 2018). Furthermore, we found that free protein is
409 required for condensate formation and coagulation (**Fig. 3E**; **Fig. 5G**), as it is driven by the introduction
410 of new bridging factors until the binding sites are saturated (Erdel & Rippe, 2018). Also other DNA
411 compacting proteins require free protein in solution for DNA condensation, which is thought to facilitate

412   dynamic and flexible DNA binding and therefore influence gene regulation (J. S. Graham et al., 2011).
413   In contrast to that, the LLPS forming protein HP1α continuously compacts DNA in absence of free
414   protein, only triggered by pre-bound HP1α (Keenen et al., 2020). DNA compaction frequently occurs in
415   DNA curtain experiments at Scc2/4 concentrations higher than 10 nM (**Fig. 2C**), which suggests that
416   the DNA needs to be coated with protein to a certain extent to induce condensate formation through a
417   coil-globule transition (Lappala & Terentjev, 2013; Quail et al., 2020; Shendruk et al., 2015). However,
418   our optical tweezer data show no linear relation between protein amount and compaction behavior as
419   higher concentrations prevent compaction dramatically (**Fig. 5H**). This might be explained by a
420   reduction of possible DNA bridging points when DNA is completely coated by Scc2/4 at concentrations
421   higher than 10 nM and confirms the existence of at least two independent DNA binding sites in Scc2/4
422   (Kurokawa & Murayama, 2020). HU protein was shown before to exhibit a comparable behavior
423   compacting DNA at low concentration by bending and reextending DNA at higher concentrations due
424   to protein filament formation (Song et al., 2016). The discrepancy between critical protein
425   concentrations for DNA condensation in DNA curtain and optical tweezer experiments might be due to
426   different incubation procedures as well as different effective DNA to protein ratios in the assays.

Bridging vs. bending

428   Besides protein-mediated DNA bridging, DNA compaction can also be caused by DNA bending which
429   alters DNA flexibility and regulates replication, recombination and gene expression (Dillon & Dorman,
430   2010; Gruber, 2014). Our optical tweezer experiments clearly show a sawtooth pattern in FECs (**Fig.
431   5D**), which is a known characteristic of DNA looping (Dame et al., 2006) as every rip during DNA
432   stretching marks a broken protein-DNA bridge. In our DNA curtain experiments, Scc2/4 binds
433   sequence-independently to the lambda DNA (**Fig. 4H,I**) (Taylor et al., 2015), but nevertheless,
434   compaction always starts from the free DNA end (**Fig. 4A,B**). This was also reported for other DNA
435   binding proteins, like HP1α (Keenen et al., 2020), FUS (Renger et al., 2021) or the transcription factor
436   Klf4 (Morin et al., 2020) as well as for ParB (T. G. W. Graham et al., 2014) and can be explained by a
437   preference of these proteins to bridge where tension is lowest and DNA is highly flexible (Baumann et
438   al., 2000; H. Kim & Loparo, 2016). Optical tweezer experiments confirmed this by increased compaction
439   at lower tension (**Fig. 5C,E,G**) as well as the fact that condensates do not re-form during DNA relaxation
440   but only at minimal tension at the beginning of each cycle (**Fig. 5D, Fig. S5C**). All these findings suggest
441   a clear compaction mechanism driven by bridging. However, our fluorescence intensity (**Fig. 4C**) and
442   tracer protein studies (**Fig. 4G**, **Fig. S4C**) suggest also an internal compaction mechanism most likely
443   caused by DNA bending (Carrivain et al., 2012) probably at the helix-turn-helix motifs (Harrington &
444   Winicov, 1994). The contribution of both, bridging and bending, to the compaction mechanism was
445   previously discovered for a bacterial SMC protein (H. Kim & Loparo, 2016). Furthermore, crystal
446   structures as well as molecular models of cohesin in complex with Scc2/4 suggest that DNA bending
447   might be an essential step for cohesin loading (Higashi et al., 2020; Shi et al., 2020). However, in optical
448   tweezer experiments, we could not resolve a reduction in DNA persistence length, which was found to
449   occur during DNA bending (Farge et al., 2012), as the bridging process dominated FEC appearance.

Loading sites for cohesin

450
451 Scc2/4-supported loading of cohesin is more efficient (Stigler et al., 2016) and more stable (Gutierrez-
452 Escribano et al., 2019) than self-loading due to a topological entrapment of the DNA (Murayama &
453 Uhlmann, 2014). Hence, we propose that phase separation might trigger this loading, as we and others
454 could not find condensate formation by cohesin in absence of Scc2/4 (**Fig. S6C**, (Ryu et al., 2021)).
455 Our DNA curtain experiments clearly show that cohesin is recruited preferably to the condensates (**Fig.**
456 **6A,B, Fig. S6A**) and that these cohesin molecules are also more resistant to high salt washes (**Fig.**
457 **6H**), which suggests a topological entrapment of the DNA (Kurokawa & Murayama, 2020) in a manner
458 that prevents sliding-off the single tethered DNA strand. Interestingly, SMC complexes that load
459 themselves on DNA like MukB (Kumar et al., 2017) and yeast condensin (Yoshimura et al., 2002) also
460 form co-condensates with DNA. Hence, our observations strongly suggest that phase separation
461 induces loading. Protein recruitment to phase separated droplets has also been observed in other
462 contexts. For example, FET-fusion proteins form condensates with DNA and recruit and activate RNA
463 polymerase even without the respective promoter (Zuo et al., 2021). Similarly, the DNA repair protein
464 ATR is recruited to and activated in condensates (Frattini et al., 2021). We therefore propose that also
465 Scc2/4 condensates do not only bind but also activate cohesin, most likely by stimulating ATPase
466 function (Murayama & Uhlmann, 2014; Petela et al., 2018).
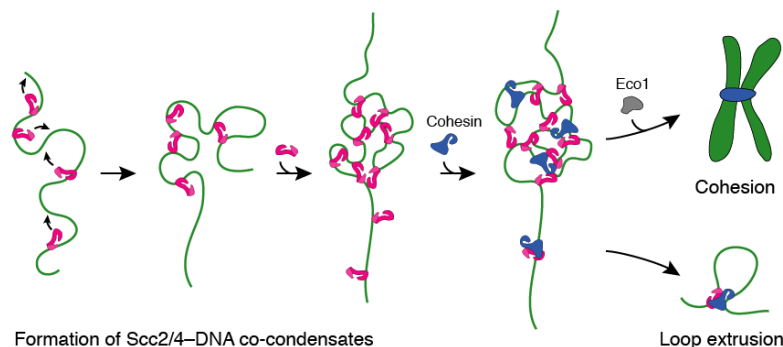
467
468 **Figure 7.** Schematic representation of DNA compaction mechanism. Scc2/4 binds randomly and bridges DNA
469 dependent on DNA tension. Free protein promotes the condensation process by providing new interaction points.
470 Cohesin is preferably recruited to the condensates creating a crowded environment which facilitates the recruitment
471 of other proteins like Eco1 and finally enables sister chromatid cohesion. Cohesin that is loaded on uncompacted
472 DNA might induce loop extrusion.

Ideas and Speculation

473
474 There are indications that TAD formation and phase separation are counteracting processes (Y. Kim &
475 Yu, 2020), raising the question whether the loading of cohesin at Scc2/4-mediated DNA-condensates
476 determines whether cohesin promotes loop extrusion or sister chromatid cohesion. As cohesin
477 degradation in vivo leads to the loss of all DNA loops but not of the condensation-mediated
478 compartmentalization of chromatin (Rao et al., 2017), it is likely that phase separation does not cause
479 loop extrusion but both processes co-exist. Furthermore, TAD formation clearly depends on ATP and
480 is hence an active process (Gutierrez-Escribano et al., 2019; Y. Kim et al., 2019), while phase
481 separation can organize DNA without energy consumption (Ryu et al., 2021). Sister chromatid

482   cohesion, in contrast, is known to start at replication forks, a very crowded environment, where most
483   likely multiple cohesins are required to resist strong tension (Skibbens, 2000; Zhang et al., 2008). It is
484   possible that loading at condensates sets a starting point to accumulate cohesin and recruit other
485   factors that are required for cohesion maintenance (**Figure 7**). An interesting candidate for such a factor
486   is the cohesin acetylase Eco1, which was previously shown to be recruitable by DNA-protein-co-
487   condensates in other contexts (Zuilkoski & Skibbens, 2020). It is possbile that Scc2/4 is exchanged by
488   these factors within the condensates once its task is fulfilled as it is known that Scc2/4 is not required
489   for cohesion maintenance (Srinivasan et al., 2019). Future studies need to reveal if and how other
490   downstream protein factors are recruited to the condensates and how interchangeable their
491   composition is. Nevertheless, our results provide new insights into the properties and the formation
492   mechanisms of protein-DNA co-condensates and prove the power of single-molecule methods to
493   uncover unexpected features of already well-known protein complexes.

Methods

Protein Expression and Purification

496   The S. cerevisiae cohesin tetramer (SMC3-SMC1-SCC1-SCC3) and loader complex Scc2/4 were
497   cloned in multicopy episomal vectors (pRS424-GAL1-10-SMC1-Strep-SM3-GAL7-SCC1-HIS-HA +
498   pRS426-GAL-Scc3; pRS426-URA3-GAL-SCC2-3xMyc-3xStrepII-SCC4) and transformed into yeast
499   W303-1a strains. Protein expression and purification was done as described before (Gutierrez-
500   Escribano et al., 2019). In brief, yeast was cultivated at 30 °C in selected dropout medium supplemented
501   with 2 % raffinose and 0.05 % glucose to an OD > 0.8, induced by addition of 2 % galactose and grown
502   for further 20 h at 20 °C. Cells were harvested by centrifugation (4500 rpm, 15 min, 4 °C), washed with
503   PBS and resuspended in buffer A (25 mM Hepes, pH 7.5, 5 % glycerol, 5 mM β-Mercaptoethanol)
504   containing 200 mM NaCl (A-200) and protease inhibitor (cOmplete, Sigma-Aldrich, St. Louis, MI). The
505   cell suspension was frozen dropwise in liquid nitrogen and stored at -80 °C overnight. The frozen yeast
506   suspension was lysed by freezer mill (SPEX sample prep, Metuchen, NY) and afterwards thawed on
507   ice. The solution was supplemented with Pierce Universal Nuclease (0.1 μl/ml, Thermo Fisher
508   Scientific, Waltham, MA) and incubated for 1 h at 4 °C while rotating. After centrifugation (17,000 xg,
509   30 min, 4 °C) and filtering (0.22 μm, Thermo Fisher Scientific), lysate was purified on a 1 ml Strep Trap
510   HP (GE Healthcare, Chicago, IL) using the Äkta pure purification system (Cytiva, Marlborough, MA)
511   and eluted by buffer A-200 containing 5 mM D-desthiobiotin (Thermo Fisher Scientific). Pooled eluate
512   fractions were adjusted to 150 mM NaCl and purified on a 5 ml HiTrap Heparin column (GE Healthcare)
513   using a linear gradient from 150 mM NaCl to 1 M NaCl in buffer A. Pooled eluate fractions were
514   concentrated, adjusted to 300 mM NaCl and purified on a Superose 6 Increase 10/300 GL (GE
515   Healthcare) using buffer A containing 300 mM NaCl. Eluate was concentrated by 100 kDa Amicon Ultra,
516   frozen in liquid nitrogen and stored at -80 °C.

517   EcoRI-E111Q mutant was cloned into a pTXB3 vector including an N-terminal 3xFLAG tag and a C-
518   terminal Intein-CBD purification tag (pTXB3-3xFLAG-EcoRI_E111Q-Intein-CBD). For expression, the
519   plasmid was transformed into E. coli Rosetta (DE3) competent cells. Bacteria were cultivated at 37 °C

520   in LB medium until OD_{600} of 0.6 was reached, followed by induction of expression by addition of 1 mM
521   IPTG and further shaking at 20 °C for 4 h. Cells were harvested by centrifugation at 4000 rpm for 10
522   min, resuspended in 20 ml resuspension buffer (20 mM Tris-HCl pH 7.5, 0.1 mM PMSF, 10 % glycerol)
523   and lysed by sonication. After centrifugation, the supernatant was transferred onto 3 ml of pre-
524   equilibrated (washing buffer: 20 mM Tris-HCl pH 8.8, 0.5 M NaCl) chitin resin, incubated for 30 min at
525   4 °C and released by gravity flow. The resin was washed with washing buffer and the protein was
526   cleaved overnight at 4°C with 10 ml cleavage buffer (20 mM Tris-HCl pH 8.8, 0.5 M NaCl, 50 mM DTT).
527   The next day, eluate was released and resin was washed with 10 ml washing buffer. Fractions
528   containing EcoRI-E111Q were pooled, dialyzed at 4 °C overnight against storage buffer (40 mM Tris-
529   HCl pH 7.5, 300 mM NaCl, 0.1 mM EDTA, 50 % glycerol, 10 mM β-Mercaptoethanol, 0.15 % Tween20)
530   and stored at -80°C.

Protein labeling

532   Scc2/4 was labeled by mixing the protein in an equimolar ratio with Qdot 705 Strep Conjugate (Thermo
533   Fisher Scientific) and incubating for 10 min on ice in BSA buffer (40 mM Tris, pH 7.5, 1 mM $MgCl_2$, 1
534   mg/ml BSA, 1 mM DTT) with 50 mM NaCl. EcoRI-E111Q and cohesin tetramer were labeled with a
535   similar protocol using the anti-Flag Qdot 705 for EcoRI-E111Q and the anti-HA Qdot 705 for cohesin,
536   both produced with the SiteClick Qdot 705 antibody labelling kit (Thermo Fisher Scientific) utilizing
537   monoclonal anti-Flag M2 antibody from mouse (Sigma-Aldrich) and anti-HA high affinity from rat
538   (Sigma-Aldrich).

Droplet Microscopy

540   Scc2/4 droplets were imaged on custom-made flow cells using a prism-type total internal reflection
541   microscope (Nikon Ti2e; Nikon, Minato, Japan) with a 60x objective (CFI P-Apochromat VC 60 x WI,
542   Nikon) in brightfield mode. For flow cell production, microscopy slides (borosilicate glass, 76x26 mm,
543   Roth, Karlsruhe, Germany) were equipped with two stripes of parafilm forming a flow channel and
544   covered with a cover slip (18x18 mm, Roth). Parafilm was melted on a 100 °C hot plate to fix the
545   assembly leading to a channel of approximately 15 μl volume. Flow cells were pre-incubated with 40 μl
546   sample buffer (40 mM Tris (pH 7.5), 50 mM NaCl, 1 mM $MgCl_2$, 1 mg/ml BSA, 1 mM DTT). Variable
547   concentrations of Scc2/4 were mixed with 30 nM linearized pUC19 (digested with NdeI restriction
548   enzyme and purified by ethanol precipitation) and 0.5 mM ATP in sample buffer (20 μl reaction volume).
549   Protein-DNA mixture was applied to the flow cell and incubated for 5 min. After this, microscopy videos
550   of appr. 20 frames for each sample were recorded in NIS Elements (Nikon) using an electron multiplying
551   charge-coupled camera (Andor iXon life, Andor Technology, Belfast, UK) with illumination times of
552   100 ms and a sample rate of 200 ms. The background signal (buffer only sample) was subtracted from
553   each video using custom-written software in Igor Pro (WaveMetrics, Lake Oswego, OR). Experiments
554   were performed at least twice for each condition.

DNA curtain assay

556   DNA curtains experiments were performed in custom made flow cells produced as described previously
557   (Greene et al., 2010). In brief, Cr barriers were deposited on fused-silica slides by e-beam lithography.

558 The sample chamber around the barriers was confined by double sided tape and covered with a cover
559 slip. The flow cell was connected to a microfluidic system containing a syringe pump and two injection
560 valves by nanoports glued on drilled holes in the fused-silica slide (UQG Optics, Cambridge, UK).
561 Sample was illuminated with a 488 nm laser (OBIS LX/LS, coherent, Santa Clara, CA) in a prism-type
562 total internal reflection microscope (Nikon Ti2e) equipped with an electron multiplying charge-coupled
563 camera (Andor iXon life) with illumination times of 100 ms and a sample rate of 200 ms. Videos were
564 recorded in NIS Elements (Nikon). For single-tethered DNA curtains, 3'-biotinylated λ-DNA (NEB,
565 Ipswich, MA) was attached to the pre-added lipid bilayer surface (DOPC, DOPE, DOPE-biotin, Otto
566 Nordwald, Hamburg, Germany) by biotin-streptavidin-biotin interaction and flow stretched over the Cr
567 barriers to arrange DNA strands in an array. For flipped DNA experiments, 5'-biotinylated λ-DNA was
568 used. For double tethered DNA, double modified λ-DNA (3'- biotinylation and 5'- digoxigenation) was
569 used. After flow stretching of the DNA over the Cr barriers, DNA was anchored to downstream Cr
570 pedestals by digoxigenin binding protein DIG10.3. All experiments were performed in BSA buffer
571 supplemented with 0.16 nM YOYO-1. Different concentrations of Scc2/4 were diluted in BSA buffer
572 containing variable amounts of NaCl (0 mM, 50 mM, 100 mM, 150 mM), 0.5 mM ATP, 100 μM biotin
573 and loaded on the DNA curtain using a continuous flow of 0.1 ml/min for 4 min. For all injections, a 50 μl
574 injection loop and 65 μl sample volume were used. On double tethered DNA curtains, protein was
575 loaded with a flow of 0.3 ml/min and incubated on the DNA for 5 min without flow. After this, unbound
576 protein was flushed out with 0.3 ml/min and remaining protein was documented. The setup for the study
577 of the condensation of mobile surface-tethered DNA was identical to the setup used for DNA curtains,
578 but videos were recorded away from the chromium barriers.

579 As DNA curtains provide information about multiple DNA molecules at once, sufficient statistics are
580 already achieved with one measurement. We repeated experiments at least once to rule out
581 experimental fluctuations and pooled results from different experiments to one data set. For very high
582 protein concentrations (300 nM) we performed DNA curtains assays only once, as then unspecific
583 protein binding increased massively preventing any further experiments in the flow cell.

584 For compaction assays with a tracer molecule, 10 nM Qdot-labeled EcoRI-E111Q was supplemented
585 with 0.5 mM ATP and 100 μM biotin in BSA buffer with 50 mM NaCl and loaded on the DNA curtains
586 with 0.1 ml/min continuous flow. After flushing out all unbound protein, 50 nM unlabeled Scc2/4 was
587 flushed into the flow cell and compaction was documented. The experiments were performed in
588 triplicates.

589 For cohesin recruitment experiments, 30 nM unlabeled Scc2/4 was loaded on the curtains first (in BSA
590 buffer with 50 mM NaCl, 0.5 mM ATP, 100 uM biotin), followed by loading of 20 nM Qdot-labeled
591 cohesin tetramer in the same buffer. For salt washes, 2M NaCl in BSA buffer was applied with a flow
592 of 0.3 ml/min. The experiments were performed in triplicates.

593 For decondensation, 100 nM Scc2/4 was loaded without laser excitation to prevent photo-crosslinking.
594 After this, 20 % 1,6-hexanediol (Sigma Aldrich) or 2 M NaCl were loaded on the DNA curtains under
595 continuous flow with laser excitation and decompaction was documented. Protein injection profiles were
596 determined by loading blue dextran in BSA buffer on the flow cell and detecting the absorption change
597 over time in brightfield microscopy.

Data analysis DNA curtains

Videos were analyzed using custom-written software in Igor Pro 8 (WaveMetrics). For determination of compaction (%), DNA length before and after protein exposure was determined manually from kymograms. Spot fluorescence over time was determined with the help of a custom-written multi particle tracker. In cohesin recruitment assays, cohesin binding events as well as the amount of cohesin molecules remaining at the DNA after salt wash were counted in dependence of Scc2/4 presence. Cohesin binding events were also counted according to the binding at loader-formed condensates or at uncompacted DNA. Cohesin stability after salt wash was determined for these subspecies separately. Data was collected in at least two independent experiments and pooled. Standard error was calculated from binomial distribution and significance was determined by a z-test. P-values were calculated from z-values assuming a two-tailed hypothesis and a significance level of 0.05 using Social Science Statistics Web Calculator.

DNA compaction simulations

The DNA was approximated by a Rouse model of 160 beads, connected by Hookean springs with a length of 100 nm and a spring constant of 0.2 pN/nm. Simulations were run by integrating the time-discretized Langevin equation of the bead motion with a diffusion coefficient of $1.1e^9$ nm^2/s and a time step of $1e^{-9}$ s for $>=1e^8$ steps. One bead was fixed in space while the other beads experienced a stretching force to extend the DNA to a mean end-to-end distance of ~10 µm, close to experimental conditions. Condensation conditions that explicitly do not change the equilibrium spacing between the beads were enabled by an additional Lennard-Jones attraction between beads with an equilibrium distance of 100 nm and a potential depth of 5 k_BT. The position of every 20th bead was recorded. Simulations were run in triplicate.

Optical tweezers

Optical tweezer experiments were performed on a dual-trap C-Trap (Lumicks, Amsterdam, The Netherlands) including a µFlow microfluidics system and a 4-channel glass slide (Type C2, Lumicks). The system was controlled using the Bluelake software (Lumicks) and custom Python scripts. The first channel of the slide contained 4.36 µm Streptavidin coated polystyrene microspheres (Spherotech, Fulda, Germany) diluted in sample buffer (40 mM Tris, pH 7.5, 1 mM MgCl$_2$, 1 mg/ml BSA, 1 mM DTT, 50 mM NaCl). Here, two microspheres were trapped and the stiffness of the optical traps was calibrated using Bluelake's built-in thermal calibration method. The microspheres were then moved to the second channel which contained 3',5'-double-biotinylated λ-DNA in BSA buffer while applying a weak flow. The mobile optical trap was moved periodically between a bead distance of 5 and 15 µm while the force acting on the trapped microsphere was observed. Upon detection of the characteristic force increase at increasing bead distances caused by a captured DNA strand, the microspheres were moved to the third channel, which contained sample buffer supplemented with 0.5 mM ATP. There, tethering of a single DNA strand was verified by recording a force-extension curve (FEC) and comparing it to an extensible worm-like-chain (eWLC) model for a single λ-DNA molecule (Wang et al., 1997).

During experiment, the DNA was stretched first to a tension of 0.3 pN and held at this trap separation for 60 s, then stretched to a tension of 0.05 pN and held at this position for 30 s. After this, force-

637   extension curves were recorded for five stretch-relax cycles. This procedure was performed first in the

638   buffer channel, then similarly in the protein channel (variable concentrations of Scc2/4 in sample buffer

639   supplemented with 0.5 mM ATP) and after this again in the buffer channel. For 10 nM Scc2/4, 15 DNA

640   tethers were analyzed by stretch-relax cycles and data points were pooled. For 30 nM and 50 nM

641   Scc2/4, 10 and 13 tethers were analyzed, respectively.

Data analysis optical tweezers

643   Analysis of the recorded incubation steps and force-extension curves was performed using custom-

644   written code for the IGOR Pro 8 software (WaveMetrics). The effect of incubation of λ-DNA with Scc2/4

645   was analyzed by comparing the change in the differential force response over time ΔF during the

646   different incubation steps. The constant trap separation d is composed of the sum of DNA extension

647    $\xi(F)$ and the bead deflection $\frac{F}{k_c}$,

$$d = \xi(F) + \frac{F}{k_c},$$

649   with F = F$_{t(0)}$ + ΔF, and k_c is the trap stiffness. F$_{t(0)}$ is the initial DNA tension, 0.3 or 0.05 pN for the two

650   incubation conditions, respectively. Rearranging the equation yields the DNA extension as

$$\xi(F) = d - \frac{F}{k_c}.$$

652   Using an inversion of the eWLC model (Wang et al., 1997), $\xi(F)$ can then be converted into a contour

653   length L_c (Mehlich et al., 2020).

654   For each DNA molecule the force-extension curves (FEC) for naked λ-DNA where fitted with an eWLC

655   model to obtain their persistence length L_p and contour length L_c. For all further analysis of the FECs,

656   the persistence length was then fixed to the value obtained for naked DNA. For every stretch FEC, the

657   contour length at each force is then obtained by applying an inverted eWLC to each point of the FEC

658   and binning the result based on the corresponding force value. The contour lengths were then

659   normalized to the previously obtained contour length of naked DNA.

660   The size of loops formed by Scc2/4 on the DNA was determined using the stretch FECs. Opening of

661   DNA loops during stretching results in a sawtooth pattern. Fitting an eWLC with fixed persistence length

662   to the FEC between two opening events, yields the respective contour length for each sawtooth feature.

663   The loop size is then obtained as the difference in contour length of two consecutive features. Loop

664   sizes were plotted in a histogram, mean was determined from bootstrapping (error = 1-σ).

Acknowledgments

Competing interests

The authors declare no competing interests.

References

Aktar, F., Burudpakdee, C., Polanco, M., Pei, S., Swayne, T. C., Lipke, P. N., & Emtage, L. (2019). The huntingtin inclusion is a dynamic phase-separated compartment. Life Science Alliance, 2(5), e201900489. https://doi.org/10.26508/lsa.201900489

André, A. A. M., & Spruijt, E. (2020). Liquid–Liquid Phase Separation in Crowded Environments. International Journal of Molecular Sciences, 21(16), 5908. https://doi.org/10.3390/ijms21165908

Bauer, B. W., Davidson, I. F., Canena, D., Wutz, G., Tang, W., Litos, G., Horn, S., Hinterdorfer, P., & Peters, J.-M. (2021). Cohesin mediates DNA loop extrusion by a "swing and clamp" mechanism. Cell, 0(0). https://doi.org/10.1016/j.cell.2021.09.016

Baumann, C. G., Bloomfield, V. A., Smith, S. B., Bustamante, C., Wang, M. D., & Block, S. M. (2000). Stretching of Single Collapsed DNA Molecules. Biophysical Journal, 78(4), 1965–1978. https://doi.org/10.1016/S0006-3495(00)76744-0

Boehning, M., Dugast-Darzacq, C., Rankovic, M., Hansen, A. S., Yu, T., Marie-Nelly, H., McSwiggen, D. T., Kokic, G., Dailey, G. M., Cramer, P., Darzacq, X., & Zweckstetter, M. (2018). RNA polymerase II clustering through carboxy-terminal domain phase separation. Nature Structural & Molecular Biology, 25(9), 833–840. https://doi.org/10.1038/s41594-018-0112-y

Boija, A., Klein, I. A., Sabari, B. R., Dall'Agnese, A., Coffey, E. L., Zamudio, A. V., Li, C. H., Shrinivas, K., Manteiga, J. C., Hannett, N. M., Abraham, B. J., Afeyan, L. K., Guo, Y. E., Rimel, J. K., Fant, C. B., Schuijers, J., Lee, T. I., Taatjes, D. J., & Young, R. A. (2018). Transcription Factors Activate Genes through the Phase-Separation Capacity of Their Activation Domains. Cell, 175(7), 1842-1855.e16. https://doi.org/10.1016/j.cell.2018.10.042

Broedersz, C. P., Wang, X., Meir, Y., Loparo, J. J., Rudner, D. Z., & Wingreen, N. S. (2014). Condensation and localization of the partitioning protein ParB on the bacterial chromosome. Proceedings of the National Academy of Sciences, 111(24), 8809–8814. https://doi.org/10.1073/pnas.1402529111

Çamdere, G., Guacci, V., Stricklin, J., & Koshland, D. (2015). The ATPases of cohesin interface with regulators to modulate cohesin-mediated DNA tethering. ELife, 4. https://doi.org/10.7554/eLife.11315

Carrivain, P., Cournac, A., Lavelle, C., Lesne, A., Mozziconacci, J., Paillusson, F., Signon, L., Victor, J.-M., & Barbi, M. (2012). Electrostatics of DNA compaction in viruses, bacteria and eukaryotes: Functional insights and evolutionary perspective. Soft Matter, 8(36), 9285. https://doi.org/10.1039/c2sm25789k

Chao, W. C. H., Murayama, Y., Muñoz, S., Costa, A., Uhlmann, F., & Singleton, M. R. (2015). Structural Studies Reveal the Functional Modularity of the Scc2-Scc4 Cohesin Loader. Cell Reports, 12(5), 719–725. https://doi.org/10.1016/j.celrep.2015.06.071

707   Chao, W. C. H., Murayama, Y., Muñoz, S., Jones, A. W., Wade, B. O., Purkiss, A. G., Hu, X.-W., Borg,
708   A., Snijders, A. P., Uhlmann, F., & Singleton, M. R. (2017). Structure of the cohesin loader
709   Scc2. Nature Communications, 8(1), 13952. https://doi.org/10.1038/ncomms13952

710   Ciosk, R., Shirayama, M., Shevchenko, A., Tanaka, T., Toth, A., Shevchenko, A., & Nasmyth, K. (2000).
711   Cohesin's Binding to Chromosomes Depends on a Separate Complex Consisting of Scc2 and
712   Scc4 Proteins. Molecular Cell, 5(2), 243–254. https://doi.org/10.1016/S1097-2765(00)80420-7

713   Collier, J. E., Lee, B.-G., Roig, M. B., Yatskevich, S., Petela, N. J., Metson, J., Voulgaris, M.,
714   Llamazares, A. G., Löwe, J., & Nasmyth, K. A. (2020). ATP dependent DNA transport within
715   cohesin: Scc2 clamps DNA on top of engaged heads while Scc3 promotes entrapment within
716   the SMC-kleisin ring. BioRxiv, 2020.06.03.132233. https://doi.org/10.1101/2020.06.03.132233

717   Dame, R. T., Noom, M. C., & Wuite, G. J. L. (2006). Bacterial chromatin organization by H-NS protein
718   unravelled   using   dual   DNA   manipulation.   Nature,   444(7117),   387–390.
719   https://doi.org/10.1038/nature05283

720   Davidson, I. F., Bauer, B., Goetz, D., Tang, W., Wutz, G., & Peters, J.-M. (2019). DNA loop extrusion
721   by human cohesin. Science, 366(6471), 1338–1345. https://doi.org/10.1126/science.aaz3418

722   Davidson, I. F., & Peters, J.-M. (2021). Genome folding through loop extrusion by SMC complexes.
723   Nature Reviews Molecular Cell Biology, 22(7), 445–464. https://doi.org/10.1038/s41580-021-
724   00349-7

725   Dignon, G. L., Best, R. B., & Mittal, J. (2020). Biomolecular Phase Separation: From Molecular Driving
726   Forces to Macroscopic Properties. Annual Review of Physical Chemistry, 71(1), 53–75.
727   https://doi.org/10.1146/annurev-physchem-071819-113553

728   Dillon, S. C., & Dorman, C. J. (2010). Bacterial nucleoid-associated proteins, nucleoid structure and
729   gene   expression.   Nature   Reviews   Microbiology,   8(3),   185–195.
730   https://doi.org/10.1038/nrmicro2261

731   Dixon, J. R., Selvaraj, S., Yue, F., Kim, A., Li, Y., Shen, Y., Hu, M., Liu, J. S., & Ren, B. (2012).
732   Topological domains in mammalian genomes identified by analysis of chromatin interactions.
733   Nature, 485(7398), 376–380. https://doi.org/10.1038/nature11082

734   Erdel, F., & Rippe, K. (2018). Formation of Chromatin Subcompartments by Phase Separation.
735   Biophysical Journal, 114(10), 2262–2270. https://doi.org/10.1016/j.bpj.2018.03.011

736   Farge, G., Laurens, N., Broekmans, O. D., van den Wildenberg, S. M. J. L., Dekker, L. C. M., Gaspari,
737   M., Gustafsson, C. M., Peterman, E. J. G., Falkenberg, M., & Wuite, G. J. L. (2012). Protein
738   sliding and DNA denaturation are essential for DNA organization by human mitochondrial
739   transcription   factor   A.   Nature   Communications,   3(1),   1013.
740   https://doi.org/10.1038/ncomms2001

741   Fisher, G. L., Pastrana, C. L., Higman, V. A., Koh, A., Taylor, J. A., Butterer, A., Craggs, T., Sobott, F.,
742   Murray, H., Crump, M. P., Moreno-Herrero, F., & Dillingham, M. S. (2017). The structural basis
743   for dynamic DNA binding and bridging interactions which condense the bacterial centromere.
744   ELife, 6, e28086. https://doi.org/10.7554/eLife.28086

745   Frattini, C., Promonet, A., Alghoul, E., Vidal-Eychenie, S., Lamarque, M., Blanchard, M.-P., Urbach, S.,
746   Basbous, J., & Constantinou, A. (2021). TopBP1 assembles nuclear condensates to switch on

747   ATR signaling. Molecular Cell, 81(6), 1231-1245.e8.
748   https://doi.org/10.1016/j.molcel.2020.12.049

749 Fudenberg, G., Abdennur, N., Imakaev, M., Goloborodko, A., & Mirny, L. A. (2017). Emerging Evidence
750   of Chromosome Folding by Loop Extrusion. Cold Spring Harbor Symposia on Quantitative
751   Biology, 82, 45–55. https://doi.org/10.1101/sqb.2017.82.034710

752 Fudenberg, G., Imakaev, M., Lu, C., Goloborodko, A., Abdennur, N., & Mirny, L. A. (2016). Formation
753   of Chromosomal Domains by Loop Extrusion. Cell Reports, 15(9), 2038–2049.
754   https://doi.org/10.1016/j.celrep.2016.04.085

755 Gallego, L. D., Schneider, M., Mittal, C., Romanauska, A., Gudino Carrillo, R. M., Schubert, T., Pugh,
756   B. F., & Köhler, A. (2020). Phase separation directs ubiquitination of gene-body nucleosomes.
757   Nature, 579(7800), 592–597. https://doi.org/10.1038/s41586-020-2097-z

758 Goloborodko, A., Marko, J. F., & Mirny, L. A. (2016). Chromosome Compaction by Active Loop
759   Extrusion. Biophysical Journal, 110(10), 2162–2168. https://doi.org/10.1016/j.bpj.2016.02.041

760 Graham, J. S., Johnson, R. C., & Marko, J. F. (2011). Concentration-dependent exchange accelerates
761   turnover of proteins bound to double-stranded DNA. Nucleic Acids Research, 39(6), 2249–
762   2259. https://doi.org/10.1093/nar/gkq1140

763 Graham, T. G. W., Wang, X., Song, D., Etson, C. M., Oijen, A. M. van, Rudner, D. Z., & Loparo, J. J.
764   (2014). ParB spreading requires DNA bridging. Genes & Development, 28(11), 1228–1238.
765   https://doi.org/10.1101/gad.242206.114

766 Greene, E. C., Wind, S., Fazio, T., Gorman, J., & Visnapuu, M.-L. (2010). DNA Curtains for High-
767   Throughput Single-Molecule Optical Imaging. Methods in Enzymology, 472, 293–315.
768   https://doi.org/10.1016/S0076-6879(10)72006-1

769 Gruber, S. (2014). Multilayer chromosome organization through DNA bending, bridging and extrusion.
770   Current Opinion in Microbiology, 22, 102–110. https://doi.org/10.1016/j.mib.2014.09.018

771 Guacci, V., Koshland, D., & Strunnikov, A. (1997). A Direct Link between Sister Chromatid Cohesion
772   and Chromosome Condensation Revealed through the Analysis of MCD1 in S. cerevisiae. Cell,
773   91(1), 47–57. https://doi.org/10.1016/S0092-8674(01)80008-8

774 Guilhas, B., Walter, J.-C., Rech, J., David, G., Walliser, N. O., Palmeri, J., Mathieu-Demaziere, C.,
775   Parmeggiani, A., Bouet, J.-Y., Gall, A. L., & Nollmann, M. (2020). ATP-Driven Separation of
776   Liquid Phase Condensates in Bacteria. Molecular Cell, 79(2), 293-303.e4.
777   https://doi.org/10.1016/j.molcel.2020.06.034

778 Gutierrez-Escribano, P., Newton, M. D., Llauró, A., Huber, J., Tanasie, L., Davy, J., Aly, I., Aramayo,
779   R., Montoya, A., Kramer, H., Stigler, J., Rueda, D. S., & Aragon, L. (2019). A conserved ATP-
780   and Scc2/4-dependent activity for cohesin in tethering DNA molecules. Science Advances,
781   5(11), eaay6804. https://doi.org/10.1126/sciadv.aay6804

782 Haarhuis, J. H. I., van der Weide, R. H., Blomen, V. A., Yáñez-Cuna, J. O., Amendola, M., van Ruiten,
783   M. S., Krijger, P. H. L., Teunissen, H., Medema, R. H., van Steensel, B., Brummelkamp, T. R.,
784   de Wit, E., & Rowland, B. D. (2017). The Cohesin Release Factor WAPL Restricts Chromatin
785   Loop Extension. Cell, 169(4), 693-707.e14. https://doi.org/10.1016/j.cell.2017.04.013

786 Haering, C. H., Farcas, A.-M., Arumugam, P., Metson, J., & Nasmyth, K. (2008). The cohesin ring
787   concatenates sister DNA molecules. Nature, 454(7202), 297–301.
788   https://doi.org/10.1038/nature07098

789 Harrington, R. E., & Winicov, I. (1994). New Concepts in Protein-DNA Recognition: Sequence-directed
790   DNA Bending and Flexibility11A glossary of abbreviations and polynucleotide notation appears
791   on p. 261. In W. E. Cohn & K. Moldave (Eds.), Progress in Nucleic Acid Research and Molecular
792   Biology (Vol. 47, pp. 195–270). Academic Press. https://doi.org/10.1016/S0079-
793   6603(08)60253-6

794 Higashi, T. L., Eickhoff, P., Simoes, J. S., Locke, J., Nans, A., Flynn, H. R., Snijders, A. P.,
795   Papageorgiou, G., O'Reilly, N., Chen, Z. A., O'Reilly, F. J., Rappsilber, J., Costa, A., &
796   Uhlmann, F. (2020). A Structure-Based Mechanism for DNA Entry into the Cohesin Ring.
797   BioRxiv. https://doi.org/10.1101/2020.04.21.052944

798 Hinshaw, S. M., Makrantoni, V., Kerr, A., Marston, A. L., & Harrison, S. C. (2015). Structural evidence
799   for Scc4-dependent localization of cohesin loading. ELife, 4, e06057.
800   https://doi.org/10.7554/eLife.06057

801 Ho, B., Baryshnikova, A., & Brown, G. W. (2018). Unification of Protein Abundance Datasets Yields a
802   Quantitative Saccharomyces cerevisiae Proteome. Cell Systems, 6(2), 192-205.e3.
803   https://doi.org/10.1016/j.cels.2017.12.004

804 Johnson, R. C., Stella, S., & Heiss, J. K. (2008). Chapter 8:Bending and Compaction of DNA by
805   Proteins. In Protein-Nucleic Acid Interactions (pp. 176–220).
806   https://doi.org/10.1039/9781847558268-00176

807 Kappel, C., Zachariae, U., Dölker, N., & Grubmüller, H. (2010). An Unusual Hydrophobic Core Confers
808   Extreme Flexibility to HEAT Repeat Proteins. Biophysical Journal, 99(5), 1596–1603.
809   https://doi.org/10.1016/j.bpj.2010.06.032

810 Keenen, M. M., Brown, D., Brennan, L. D., Renger, R., Khoo, H., Carlson, C. R., Huang, B., Grill, S. W.,
811   Narlikar, G. J., & Redding, S. (2020). HP1 proteins compact DNA into mechanically and
812   positionally stable phase separated domains. BioRxiv, 2020.10.30.362772.
813   https://doi.org/10.1101/2020.10.30.362772

814 Kent, S., Brown, K., Yang, C., Alsaihati, N., Tian, C., Wang, H., & Ren, X. (2020). Phase-Separated
815   Transcriptional Condensates Accelerate Target-Search Process Revealed by Live-Cell Single-
816   Molecule Imaging. Cell Reports, 33(2), 108248. https://doi.org/10.1016/j.celrep.2020.108248

817 Kikuchi, S., Borek, D. M., Otwinowski, Z., Tomchick, D. R., & Yu, H. (2016). Crystal structure of the
818   cohesin loader Scc2 and insight into cohesinopathy. Proceedings of the National Academy of
819   Sciences, 113(44), 12444–12449. https://doi.org/10.1073/pnas.1611333113

820 Kilic, S., Lezaja, A., Gatti, M., Bianco, E., Michelena, J., Imhof, R., & Altmeyer, M. (2019). Phase
821   separation of 53BP1 determines liquid-like behavior of DNA repair compartments. The EMBO
822   Journal, 38(16), e101379. https://doi.org/10.15252/embj.2018101379

823 Kim, H., & Loparo, J. J. (2016). Multistep assembly of DNA condensation clusters by SMC. Nature
824   Communications, 7(1), 10200. https://doi.org/10.1038/ncomms10200

825 Kim, Y., Shi, Z., Zhang, H., Finkelstein, I. J., & Yu, H. (2019). Human cohesin compacts DNA by loop
826   extrusion. Science, 366(6471), 1345–1349. https://doi.org/10.1126/science.aaz4475

827 Kim, Y., & Yu, H. (2020). Shaping of the 3D genome by the ATPase machine cohesin. Experimental &
828   Molecular Medicine, 52(12), 1891–1897. https://doi.org/10.1038/s12276-020-00526-2

829 Kumar, R., Grosbart, M., Nurse, P., Bahng, S., Wyman, C. L., & Marians, K. J. (2017). The bacterial
830   condensin MukB compacts DNA by sequestering supercoils and stabilizing topologically
831   isolated loops. The Journal of Biological Chemistry, 292(41), 16904–16920.
832   https://doi.org/10.1074/jbc.M117.803312

833 Kurokawa, Y., & Murayama, Y. (2020). DNA Binding by the Mis4Scc2 Loader Promotes Topological
834   DNA Entrapment by the Cohesin Ring. Cell Reports, 33(6).
835   https://doi.org/10.1016/j.celrep.2020.108357

836 Ladouceur, A.-M., Parmar, B. S., Biedzinski, S., Wall, J., Tope, S. G., Cohn, D., Kim, A., Soubry, N.,
837   Reyes-Lamothe, R., & Weber, S. C. (2020). Clusters of bacterial RNA polymerase are
838   biomolecular condensates that assemble through liquid–liquid phase separation. Proceedings
839   of the National Academy of Sciences of the United States of America, 117(31), 18540–18549.
840   https://doi.org/10.1073/pnas.2005019117

841 Lappala, A., & Terentjev, E. M. (2013). "Raindrop" Coalescence of Polymer Chains during Coil–Globule
842   Transition. Macromolecules, 46(3), 1239–1247. https://doi.org/10.1021/ma302364f

843 Larson, A. G., Elnatan, D., Keenen, M. M., Trnka, M. J., Johnston, J. B., Burlingame, A. L., Agard, D.
844   A., Redding, S., & Narlikar, G. J. (2017). Liquid droplet formation by HP1α suggests a role for
845   phase separation in heterochromatin. Nature, 547(7662), 236–240.
846   https://doi.org/10.1038/nature22822

847 Madariaga-Marcos, J., Pastrana, C. L., Fisher, G. L., Dillingham, M. S., & Moreno-Herrero, F. (2019).
848   ParB dynamics and the critical role of the CTD in DNA condensation unveiled by combined
849   force-fluorescence measurements. ELife, 8, e43812. https://doi.org/10.7554/eLife.43812

850 Mehlich, A., Fang, J., Pelz, B., Li, H., & Stigler, J. (2020). Slow Transition Path Times Reveal a Complex
851   Folding Barrier in a Designed Protein. Frontiers in Chemistry, 8, 1103.
852   https://doi.org/10.3389/fchem.2020.587824

853 Mészáros, B., Erdős, G., & Dosztányi, Z. (2018). IUPred2A: Context-dependent prediction of protein
854   disorder as a function of redox state and protein binding. Nucleic Acids Research, 46(W1),
855   W329–W337. https://doi.org/10.1093/nar/gky384

856 Michaelis, C., Ciosk, R., & Nasmyth, K. (1997). Cohesins: Chromosomal Proteins that Prevent
857   Premature Separation of Sister Chromatids. Cell, 91(1), 35–45. https://doi.org/10.1016/S0092-
858   8674(01)80007-6

859 Minamino, M., Higashi, T. L., Bouchoux, C., & Uhlmann, F. (2018). Topological in vitro loading of the
860   budding yeast cohesin ring onto DNA. Life Science Alliance, 1(5).
861   https://doi.org/10.26508/lsa.201800143

862 Minnen, A., Attaiech, L., Thon, M., Gruber, S., & Veening, J.-W. (2011). SMC is recruited to oriC by
863   ParB and promotes chromosome segregation in Streptococcus pneumoniae. Molecular
864   Microbiology, 81(3), 676–688. https://doi.org/10.1111/j.1365-2958.2011.07722.x

865 Mitrea, D. M., Chandra, B., Ferrolino, M. C., Gibbs, E. B., Tolbert, M., White, M. R., & Kriwacki, R. W.
866   (2018). Methods for Physical Characterization of Phase-Separated Bodies and Membrane-less
867   Organelles.   Journal   of   Molecular   Biology,   430(23),   4773–4805.
868   https://doi.org/10.1016/j.jmb.2018.07.006

869 Morin, J. A., Wittmann, S., Choubey, S., Klosin, A., Golfier, S., Hyman, A. A., Jülicher, F., & Grill, S. W.
870   (2020). Surface condensation of a pioneer transcription factor on DNA. BioRxiv,
871   2020.09.24.311712. https://doi.org/10.1101/2020.09.24.311712

872 Murayama, Y., & Uhlmann, F. (2014). Biochemical reconstitution of topological DNA binding by the
873   cohesin ring. Nature, 505(7483), 367–371. https://doi.org/10.1038/nature12867

874 Oudet, P., Gross-Bellard, M., & Chambon, P. (1975). Electron microscopic and biochemical evidence
875   that chromatin structure is a repeating unit. Cell, 4(4), 281–300. https://doi.org/10.1016/0092-
876   8674(75)90149-x

877 Parker, M. W., Bell, M., Mir, M., Kao, J. A., Darzacq, X., Botchan, M. R., & Berger, J. M. (2019). A new
878   class of disordered elements controls DNA replication through initiator self-assembly. ELife, 8,
879   e48562. https://doi.org/10.7554/eLife.48562

880 Petela, N. J., Gligoris, T. G., Metson, J., Lee, B.-G., Voulgaris, M., Hu, B., Kikuchi, S., Chapard, C.,
881   Chen, W., Rajendra, E., Srinivisan, M., Yu, H., Löwe, J., & Nasmyth, K. A. (2018). Scc2 Is a
882   Potent Activator of Cohesin's ATPase that Promotes Loading by Binding Scc1 without Pds5.
883   Molecular Cell, 70(6), 1134-1148.e7. https://doi.org/10.1016/j.molcel.2018.05.022

884 Pombo, A., & Dillon, N. (2015). Three-dimensional genome architecture: Players and mechanisms.
885   Nature Reviews Molecular Cell Biology, 16(4), 245–257. https://doi.org/10.1038/nrm3965

886 Pope, B. D., Ryba, T., Dileep, V., Yue, F., Wu, W., Denas, O., Vera, D. L., Wang, Y., Hansen, R. S.,
887   Canfield, T. K., Thurman, R. E., Cheng, Y., Gülsoy, G., Dennis, J. H., Snyder, M. P.,
888   Stamatoyannopoulos, J. A., Taylor, J., Hardison, R. C., Kahveci, T., … Gilbert, D. M. (2014).
889   Topologically associating domains are stable units of replication-timing regulation. Nature,
890   515(7527), 402–405. https://doi.org/10.1038/nature13986

891 Quail, T., Golfier, S., Elsner, M., Ishihara, K., Jülicher, F., & Brugués, J. (2020). Capillary forces drive
892   pioneer transcription factor-mediated DNA condensation. BioRxiv, 2020.09.17.302299.
893   https://doi.org/10.1101/2020.09.17.302299

894 Rao, S. S. P., Huang, S.-C., Hilaire, B. G. S., Engreitz, J. M., Perez, E. M., Kieffer-Kwon, K.-R., Sanborn,
895   A. L., Johnstone, S. E., Bascom, G. D., Bochkov, I. D., Huang, X., Shamim, M. S., Shin, J.,
896   Turner, D., Ye, Z., Omer, A. D., Robinson, J. T., Schlick, T., Bernstein, B. E., … Aiden, E. L.
897   (2017). Cohesin Loss Eliminates All Loop Domains. Cell, 171(2), 305-320.e24.
898   https://doi.org/10.1016/j.cell.2017.09.026

899 Razin, S. V., & Ulianov, S. V. (2020). Divide and Rule: Phase Separation in Eukaryotic Genome
900   Functioning. Cells, 9(11). https://doi.org/10.3390/cells9112480

901 Renger, R., Morin, J. A., Lemaitre, R., Ruer-Gruss, M., Jülicher, F., Hermann, A., & Grill, S. W. (2021).
902   Co-condensation of proteins with single- and double-stranded DNA. BioRxiv,
903   2021.03.17.435834. https://doi.org/10.1101/2021.03.17.435834

904   Rhodes, J., Mazza, D., Nasmyth, K., & Uphoff, S. (2017). Scc2/Nipbl hops between chromosomal
905   cohesin rings after loading. ELife, 6, e30000. https://doi.org/10.7554/eLife.30000

906   Ryu, J.-K., Bouchoux, C., Liu, H. W., Kim, E., Minamino, M., Groot, R. de, Katan, A. J., Bonato, A.,
907   Marenduzzo, D., Michieletto, D., Uhlmann, F., & Dekker, C. (2021). Bridging-induced phase
908   separation induced by cohesin SMC protein complexes. Science Advances, 7(7), eabe5905.
909   https://doi.org/10.1126/sciadv.abe5905

910   Sabari, B. R., Dall'Agnese, A., Boija, A., Klein, I. A., Coffey, E. L., Shrinivas, K., Abraham, B. J., Hannett,
911   N. M., Zamudio, A. V., Manteiga, J. C., Li, C. H., Guo, Y. E., Day, D. S., Schuijers, J., Vasile,
912   E., Malik, S., Hnisz, D., Lee, T. I., Cisse, I. I., … Young, R. A. (2018). Coactivator condensation
913   at super-enhancers links phase separation and gene control. Science (New York, N.Y.),
914   361(6400). https://doi.org/10.1126/science.aar3958

915   Shendruk, T. N., Bertrand, M., de Haan, H. W., Harden, J. L., & Slater, G. W. (2015). Simulating the
916   Entropic Collapse of Coarse-Grained Chromosomes. Biophysical Journal, 108(4), 810–820.
917   https://doi.org/10.1016/j.bpj.2014.11.3487

918   Shi, Z., Gao, H., Bai, X., & Yu, H. (2020). Cryo-EM structure of the human cohesin-NIPBL-DNA
919   complex. Science, 368(6498), 1454–1459. https://doi.org/10.1126/science.abb0981

920   Skibbens, R. V. (2000). Holding Your Own: Establishing Sister Chromatid Cohesion. Genome
921   Research, 10(11), 1664–1671. https://doi.org/10.1101/gr.153600

922   Song, D., Graham, T. G. W., & Loparo, J. J. (2016). A general approach to visualize protein binding and
923   DNA conformation without protein labelling. Nature Communications, 7(1), 10976.
924   https://doi.org/10.1038/ncomms10976

925   Srinivasan, M., Petela, N. J., Scheinost, J. C., Collier, J., Voulgaris, M., B Roig, M., Beckouët, F., Hu,
926   B., & Nasmyth, K. A. (2019). Scc2 counteracts a Wapl-independent mechanism that releases
927   cohesin from chromosomes during G1. ELife, 8, e44736. https://doi.org/10.7554/eLife.44736

928   Stigler, J., Çamdere, G. Ö., Koshland, D. E., & Greene, E. C. (2016). Single-Molecule Imaging Reveals
929   a Collapsed Conformational State for DNA-Bound Cohesin. Cell Reports, 15(5), 988–998.
930   https://doi.org/10.1016/j.celrep.2016.04.003

931   Strom, A. R., Emelyanov, A. V., Mir, M., Fyodorov, D. V., Darzacq, X., & Karpen, G. H. (2017). Phase
932   separation drives heterochromatin domain formation. Nature, 547(7662), 241–245.
933   https://doi.org/10.1038/nature22989

934   Sullivan, N. L., Marquis, K. A., & Rudner, D. Z. (2009). Recruitment of SMC to the origin by ParB-parS
935   organizes the origin and promotes efficient chromosome segregation. Cell, 137(4), 697–707.
936   https://doi.org/10.1016/j.cell.2009.04.044

937   Szabo, Q., Bantignies, F., & Cavalli, G. (2019). Principles of genome folding into topologically
938   associating   domains.   Science   Advances,   5(4),   eaaw1668.
939   https://doi.org/10.1126/sciadv.aaw1668

940   Taylor, J. A., Pastrana, C. L., Butterer, A., Pernstich, C., Gwynn, E. J., Sobott, F., Moreno-Herrero, F.,
941   & Dillingham, M. S. (2015). Specific and non-specific interactions of ParB with DNA:
942   Implications for chromosome segregation. Nucleic Acids Research, 43(2), 719–731.
943   https://doi.org/10.1093/nar/gku1295

944   Verdile, V., De Paola, E., & Paronetto, M. P. (2019). Aberrant Phase Transitions: Side Effects and Novel
945   Therapeutic   Strategies   in   Human   Disease.   Frontiers   in   Genetics,   10.
946   https://doi.org/10.3389/fgene.2019.00173

947   Wang, M. D., Yin, H., Landick, R., Gelles, J., & Block, S. M. (1997). Stretching DNA with optical
948   tweezers.   Biophysical   Journal,   72(3),   1335–1346.   https://doi.org/10.1016/S0006-
949   3495(97)78780-0

950   Wei, M.-T., Chang, Y.-C., Shimobayashi, S. F., Shin, Y., Strom, A. R., & Brangwynne, C. P. (2020).
951   Nucleated transcriptional condensates amplify gene expression. Nature Cell Biology, 22(10),
952   1187–1196. https://doi.org/10.1038/s41556-020-00578-6

953   Yoshimura, S. H., & Hirano, T. (2016). HEAT repeats – versatile arrays of amphiphilic helices working
954   in   crowded   environments?   Journal   of   Cell   Science,   129(21),   3963–3970.
955   https://doi.org/10.1242/jcs.185710

956   Yoshimura, S. H., Hizume, K., Murakami, A., Sutani, T., Takeyasu, K., & Yanagida, M. (2002).
957   Condensin Architecture and Interaction with DNA: Regulatory Non-SMC Subunits Bind to the
958   Head of SMC Heterodimer. Current Biology, 12(6), 508–513. https://doi.org/10.1016/S0960-
959   9822(02)00719-4

960   Zhang, N., Kuznetsov, S. G., Sharan, S. K., Li, K., Rao, P. H., & Pati, D. (2008). A handcuff model for
961   the   cohesin   complex.   The   Journal   of   Cell   Biology,   183(6),   1019–1031.
962   https://doi.org/10.1083/jcb.200801157

963   Zhou, H., Song, Z., Zhong, S., Zuo, L., Qi, Z., Qu, L.-J., & Lai, L. (2019). Mechanism of DNA-Induced
964   Phase Separation for Transcriptional Repressor VRN1. Angewandte Chemie International
965   Edition, 58(15), 4858–4862. https://doi.org/10.1002/anie.201810373

966   Zuilkoski, C. M., & Skibbens, R. V. (2020). PCNA promotes context-specific sister chromatid cohesion
967   establishment separate from that of chromatin condensation. Cell Cycle, 19(19), 2436–2450.
968   https://doi.org/10.1080/15384101.2020.1804221

969   Zuo, L., Zhang, G., Massett, M., Cheng, J., Guo, Z., Wang, L., Gao, Y., Li, R., Huang, X., Li, P., & Qi,
970   Z. (2021). Loci-specific phase separation of FET fusion oncoproteins promotes gene
971   transcription. Nature Communications, 12(1), 1491. https://doi.org/10.1038/s41467-021-
972   21690-7

973

974

975 # Supplementary Figures

976
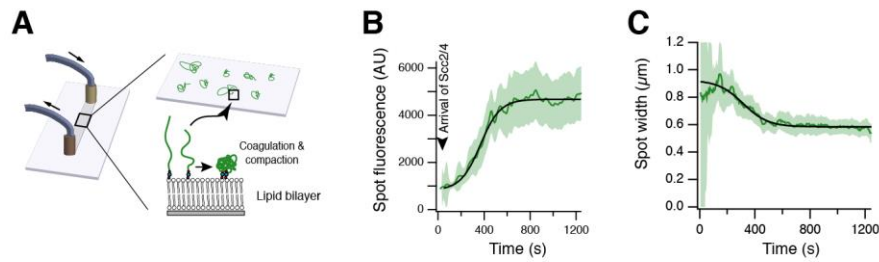
977

978 **Figure S1.** Scc2/4-mediated DNA compaction over time. (**A**) Scheme of flow cell set-up and DNA diffusion on lipid
979 bilayer. (**B**) Fluorescence intensity of freely diffusing DNA spots over time. (**C**) Change in width of freely diffusing
980 DNA spots over time. (**B+C**) Dark green curve shows the average of 154 DNA molecules, shading represents 95
981 % confidence interval.

982

983

984

985
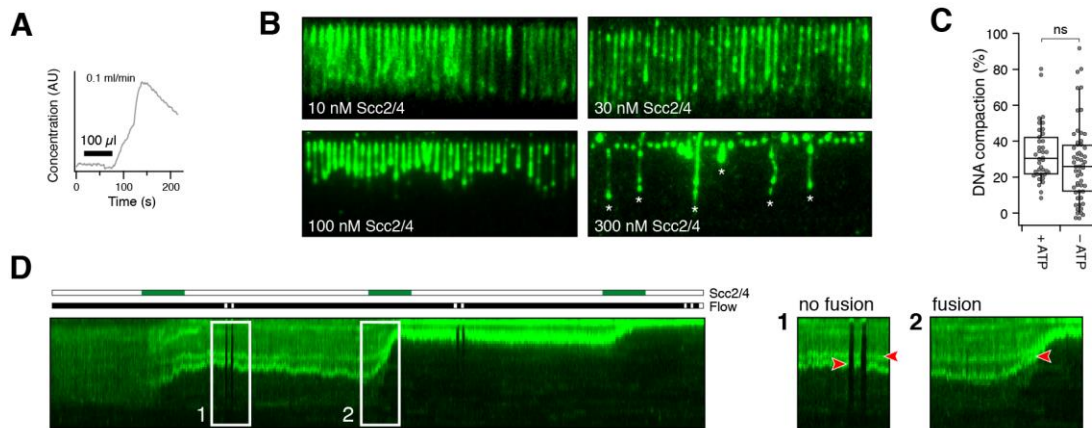
986

987 **Figure S2.** DNA compaction details. (**A**) Injection profile of 50 µl blue dextran with 0.1 ml/min flow measured by
988 change in absorption. Sample arrives after ~120s in the flow cell, maximum sample concentration: ~150 s after
989 injection. (**B**) DNA curtain experiments of different concentrations of unlabeled Scc2/4 at 50 mM NaCl to visualize
990 differences in compaction. At 300 nM Scc2/4 some DNA strands are tethered to the lipid surface (asterisks), which
991 were excluded from the analysis. (**C**) DNA compaction mediated by 30 nM Scc2/4 at 50 mM NaCl in presence or
992 absence of 0.5 mM ATP. The means are similar according to student's t-test (p-value = 0.175), $n_{(+ATP)}$=38,
993 $n_{(-ATP)}$=55. (**D**) Pulsed injection of 3x 50 µl 30 nM Scc2/4. Box 1: Condensates stay separate in absence of Scc2/4
994 even when the flow is stopped. Box 2: Condensates fuse when free Scc2/4 is present in the flow cell.

995
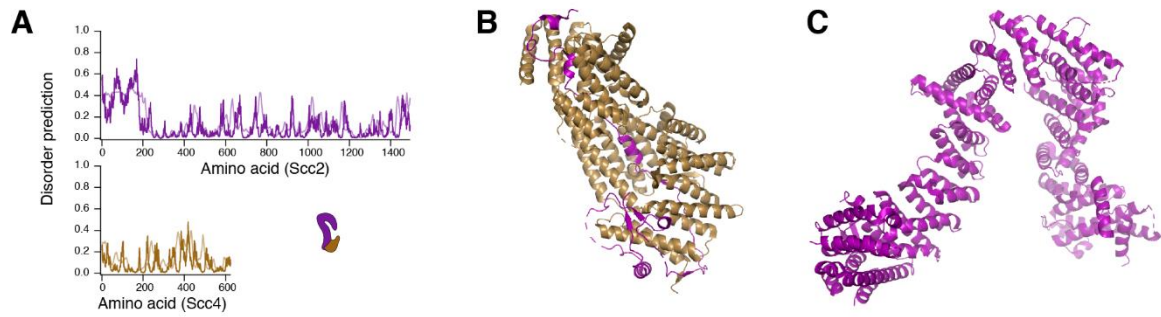
996

997 **Figure S3.** Structural insights into Scc2/4 complex. (**A**) Disorder prediction for Scc2/4 by IUPred2 (dark shading)

998 and ANCHOR2 (light shading) (Mészáros et al., 2018) (**B**) Crystal structure of Scc4 in complex with Scc2(1-181),

999 PDB: 4XDN (Hinshaw et al., 2015). The N-terminal unstructured domain of Scc2 is stabilized by Scc4. (**C**) Crystal

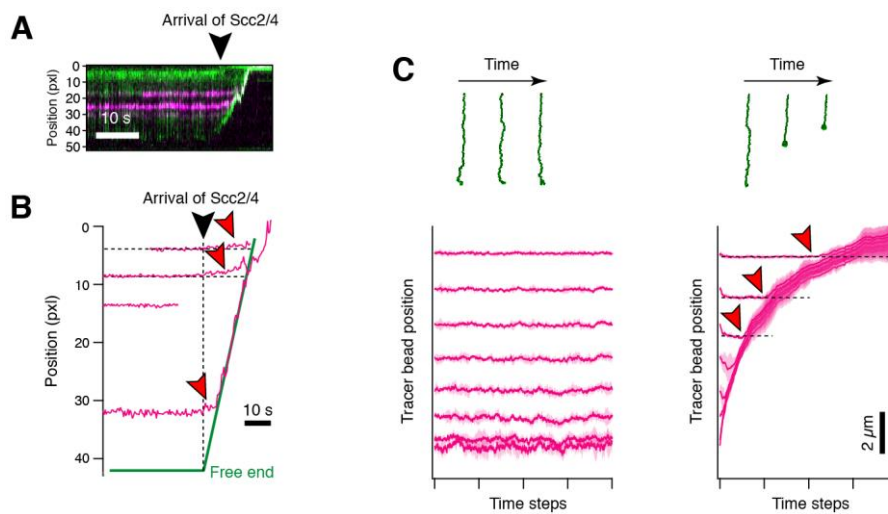1000 structure of Scc2(127-1493), PDB: 5ME3 (Chao et al., 2017).

1001

1002

1003

1004

1005

1006

1007 **Figure S4.** Internal DNA compaction. (**A**) Representative kymogram of Scc2/4-mediated DNA compaction with two

1008 EcoRI-E111Q tracer proteins (magenta) bound. (**B**) Tracked positions of tracer proteins upon Scc2/4 addition. The

1009 red arrows show movement of internal tracers distant from the condensing end. (**C**) Coarse-grained molecular

1010 dynamics simulations. Lambda DNA was represented with a Rouse model of 160 beads that were connected by

1011 segment lengths of ~300 bp. Flow-stretching force was applied. Left: naked DNA, DNA is not compacted over time.

1012 Right: DNA with Scc2/4, which was modeled by introducing an attractive Lennard-Jones-like potential between the

1013 beads, DNA is compacted over time. Red arrows indicate the internal beads, which, unlike in experimental data

1014 (see (**C**)), do not move. Shaded areas indicate the standard deviation of triplicate simulation runs.

1015
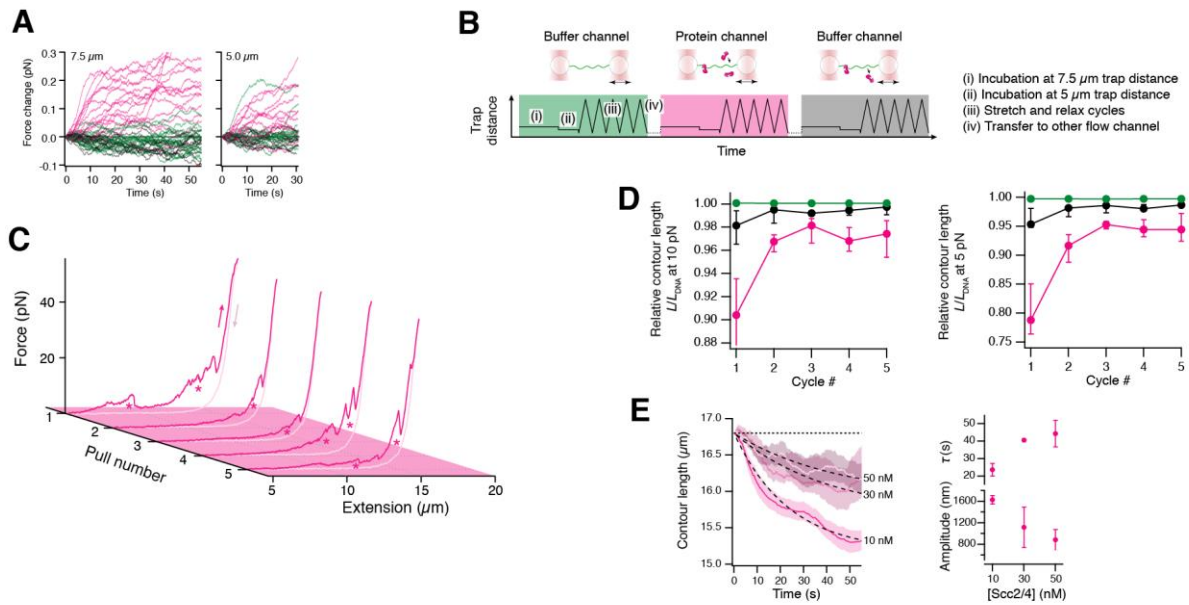
Figure S5. DNA compaction studied by optical tweezers. (**A**) Individual transient force responses of 15 lambda DNA molecules held at constant trap separation at the indicated initial forces. Green: without Scc2/4. Magenta: with 10 nM Scc2/4. Black: buffer wash after initial incubation with Scc2/4. Cf. **Fig. 5A**. (**B**) Experimental workflow. (**C**) Subsequent pulls of lambda DNA in a channel with 10 nM Scc2/4. The characteristic sawtooth pattern reforms in every cycle, observed compaction is marked by asterisks. (**D**) Relative compaction of tethers, as a function of pulling cycles. As loop formation is not instantaneous, the first cycle is significantly more compacted than the subsequent ones. (**E**) Time-dependent reduction of the tether contour length hold at 7.5 µm at different protein concentrations. Magenta traces represent averages. Dashed lines are fits to an exponential. Right: Amplitude and time constant of the exponential decrease in contour length.
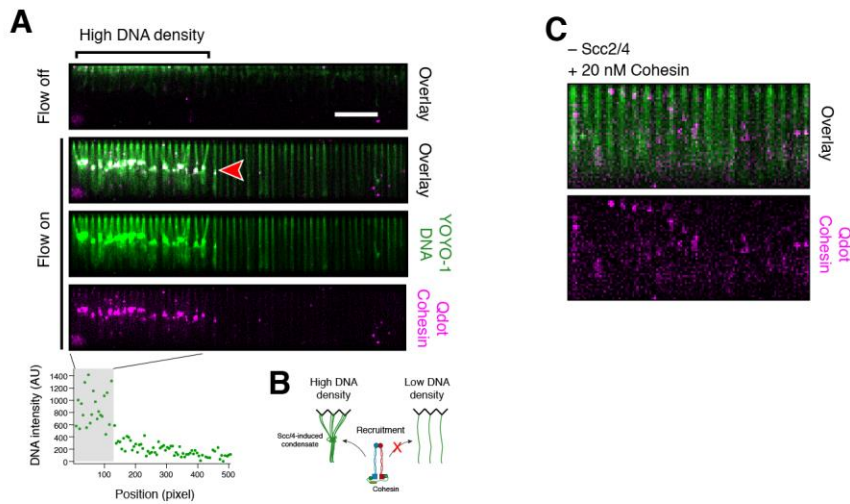
1032

Figure S6. Cohesin binding behavior on DNA curtains. (**A**) 2 nM Qdot-labeled cohesin (magenta) and 8 nM Scc2/4 (dark) were applied simultaneously to single tethered DNA curtains (green) with a flow of 0.3 ml/min followed by incubation for 5 min without flow. Cohesin loading occurred primarily at dense DNA clusters created by Scc2/4-mediated condensation. DNA density was determined by fluorescence intensity. (**B**) Model for cohesin recruitment to Scc2/4-DNA co-condensates. (**C**) DNA curtain experiment without Scc2/4. 20 nM Qdot-labeled cohesin (magenta) were applied to single tethered DNA curtains (green) under continuous flow of 0.1 ml/min. Only few binding events occurred.